

NORTH ATLANTIC TREATY ORGANIZATION
ADVISORY GROUP FOR AEROSPACE RESEARCH AND DEVELOPMENT
(ORGANISATION DU TRAITE DE L'ATLANTIQUE NORD)

AGARDograph No.172

DYNAMIC STALL

by

P.Crimi

Avco Systems Division,
Wilmington, Massachusetts 01887, USA

Edited by

P.F.Yaggy

US Army Air Mobility Research and Development Laboratory,
Moffett Field, California, USA

THE MISSION OF AGARD

The mission of AGARD is to bring together the leading personalities of the NATO nations in the fields of science and technology relating to aerospace for the following purposes:

- Exchanging of scientific and technical information;
- Continuously stimulating advances in the aerospace sciences relevant to strengthening the common defence posture;
- Improving the co-operation among member nations in aerospace research and development;
- Providing scientific and technical advice and assistance to the North Atlantic Military Committee in the field of aerospace research and development;
- Rendering scientific and technical assistance, as requested, to other NATO bodies and to member nations in connection with research and development problems in the aerospace field;
- Providing assistance to member nations for the purpose of increasing their scientific and technical potential;
- Recommending effective ways for the member nations to use their research and development capabilities for the common benefit of the NATO community.

The highest authority within AGARD is the National Delegates Board consisting of officially appointed senior representatives from each member nation. The mission of AGARD is carried out through the Panels which are composed of experts appointed by the National Delegates, the Consultant and Exchange Program and the Aerospace Applications Studies Program. The results of AGARD work are reported to the member nations and the NATO Authorities through the AGARD series of publications of which this is one.

Participation in AGARD activities is by invitation only and is normally limited to citizens of the NATO nations.

The material in this publication has been reproduced directly from copy supplied by AGARD or the author.

Published November 1973

533.6.013.66:533.662.6



*Printed by Technical Editing and Reproduction Ltd
Harford House, 7–9 Charlotte St, London. W1P 1HD*

CONTENTS

	Page
SUMMARY	1
LIST OF SYMBOLS	1
1. INTRODUCTION	4
2. PROBLEMS IN MODELLING DYNAMIC STALL	6
Stall Mechanisms and Flow Elements	6
Unsteady Separation	7
Stall Onset and Unstall Processes	8
Other Factors	9
3. ANALYTICAL REPRESENTATION OF FLOW ELEMENTS	9
General Approach – Assumptions and Limitations	9
Potential Flow	9
Boundary Layer	14
Trapped-Air Region	17
Leading-Edge Bubble	21
Computation Procedure	21
4. RESULTS FOR PRESCRIBED AIRFOIL MOTIONS	23
Transient Pitching Motions – Static Stall Characteristics	23
Sinusoidal Pitching Motions	25
5. APPLICATIONS TO HELICOPTER AEROELASTIC PROBLEMS	25
Analysis of Wake-Induced Stall	25
Analysis of Stall Flutter	27
6. RECOMMENDATIONS FOR FURTHER RESEARCH	33
Unsteady Viscous Effects	33
Leading-Edge Bubble	33
Stall Onset and Unstall Processes	33
7. REFERENCES	33
Acknowledgements	35
APPENDIX A SOLUTION FOR STALLED FLAT PLATE IN STEADY FLOW	A1-1
APPENDIX B DETERMINATION OF COUPLING PARAMETERS	B1-1

DYNAMIC STALL

by

Peter Crimi
 Leader, Special Projects Group
 Avco Systems Division
 201 Lowell Street
 Wilmington, Massachusetts 01887
 U.S.A.

SUMMARY

Problems associated with unsteady stall are summarized and past experimental and theoretical studies, relating primarily to dynamic stall of helicopter rotor blades, are reviewed. The problems attendant to analytic treatment of dynamic stall, including identification of relevant flow elements and definition of unsteady separation, are then discussed, and the basis for a theory which accounts for viscous effects and viscous-inviscid interactions analytically is presented. Results of computations are compared with measured loading on an airfoil undergoing sinusoidal pitching motion. The amounts of lift overshoot and their variation with frequency are in good agreement. Analyses of wake-induced stall and stall flutter of a helicopter rotor blade are then presented. The results indicate that the large stall-related torsional oscillations which commonly limit helicopter forward speed are the response to rapid changes in aerodynamic moment which accompany stall and unstall, rather than the consequence of an aeroelastic instability.

LIST OF SYMBOLS

a	distance aft of midchord of pitch axis in semichords
b	airfoil semichord
C	section camber distribution
C_l	lift coefficient, $C_l = 1/(\rho U^2 b)$
C_m	moment coefficient, $C_m = m/(2 \rho U^2 b^2)$
C_n	normal-force coefficient, $C_n = n/(\rho U^2 b)$
C_p	pressure coefficient, $C_p = 2(p - p_\infty)/(\rho U^2)$
c	airfoil chord
H	shear layer shape factor, $H = \theta/\delta^*$
h	section plunging velocity
J	shear layer parameter, $J = \theta^*/\delta^*$
K_θ	reciprocal turbulent Reynolds number, $K_\theta = \epsilon_m/u_e \theta$
k	reduced frequency, $k = \omega b/U$
l	lift per unit span
l_s	length of dead-air region
m	moment per unit span about pitch axis, positive to increase θ_p
N_γ	number of coefficients in series representation of γ
N_η	number of grid points in the η -direction
N_σ	number of source elements
n	force component normal to chord line per unit span
p	pressure

\bar{p}	dimensionless pressure, $\bar{p} = p / \rho U_o^2$
q_e	magnitude of flow external to boundary layer
q_s	ratio of streamwise boundary-layer flow component to U_o
q_η	ratio of normal boundary-layer flow component to U_o / Re_b
R	rotor radius
$Re()$	Reynolds number based on length indicated by subscript and U_o , unless otherwise noted
\bar{R}	integral over shear layer, $\bar{R} = (2 U_o / K_\theta H u_e) \int_0^\delta (\tau / \rho u_e^2) (\partial q_s / \partial y) dy$
r_a	inner radius of blade lifting surface
r_o	leading-edge radius
r_R	aerodynamic reference radius
s	streamwise boundary-layer coordinate
s_m	m^{th} streamwise boundary-layer grid point
T	section thickness distribution
TM	rotor blade torsional moment
t	time
\bar{t}	dimensionless time, $\bar{t} = U_o t / b$
U	instantaneous free-stream speed
U_o	reference velocity
u	flow perturbation in x-direction
u_e	flow external to viscous mixing region
v	flow perturbation in y-direction
(x, y)	coordinate system with origin at midchord of mean position of airfoil
x_m	distance aft of elastic axis of blade section mass center
x_o	value of x at the terminus of the vortex wake
Y	ordinate of airfoil surface with respect to chordline
Z_β	generalized coordinate of 2-D system, equivalent to tip displacement due to flapping (semichords)
Z_θ	generalized coordinate of 2-D system, equivalent to tip displacement due to bending (semichords)
α	angle of attack
γ	bound vortex strength
γ_2	second-order correction to the vortex strength
γ_w	wake vortex strength
ΔC_p	$C_{pL} - C_{pU}$
ΔP	$P_L - P_U$
δ	boundary layer thickness defined as distance from surface at which $U_o q_s = 0.995 q_e$
δ^*	boundary layer or shear layer displacement thickness

$\bar{\delta}$	$\delta \sqrt{Re_b}/b$
$\bar{\delta}^*$	$\delta^* \sqrt{Re_b}/b$
ϵ	eddy viscosity
η	dimensionless boundary layer coordinate, ratio of distance from the surface to $b/\sqrt{Re_b}$
n_n	n^{th} normal boundary-layer grid point
θ	boundary layer or shear layer displacement thickness
θ_1	angular displacement of 2-D system equivalent to tip displacement due to torsion (rad)
θ_p	pitch angle
θ_o	collective pitch angle
θ^*	shear layer energy thickness
Λ	pressure gradient parameter, $\Lambda = -(\delta^2 \partial p / \partial x) / (\mu q_e)$
μ	advance ratio, ratio of forward speed to ΩR
ν	kinematic viscosity
$\bar{\nu}_e$	$1 + \epsilon / \nu$
ρ	air density
σ	strength of source distribution representing trapped-air region
σ_o	total source strength representing airfoil thickness and trapped-air region
σ_2	second-order correction to the source strength
τ	shear stress
ϕ	perturbation velocity potential
ψ	rotor blade azimuth angle, measured from downwind direction
Ω	rotor rotational speed
Ω^*	dimensionless rotor speed, $\Omega^* = \Omega R / (\omega_{\theta_o} b)$
ω	angular frequency of oscillation
ω_f	flutter frequency
ω_{θ_o}	frequency of first uncoupled, nonrotating torsion mode
ω_{ϕ_o}	frequency of first uncoupled, nonrotating flapwise bending mode

Subscripts:

b	point at which pressure recovery begins in viscous mixing region
c / 4	quarter-chord point
L	lower surface of airfoil
lam	laminar
R	point of reattachment of turbulent shear layer
s	separation point
t	transition point
turb	turbulent

U upper surface of airfoil
 ∞ free stream

1. INTRODUCTION

Unsteady stall and separation phenomena have been receiving considerable attention due to recent developments in two widely separated areas. The introduction of gas turbine power in helicopters and the evolution of rotor blade design have effectively removed the power limitation from helicopter performance. One of the more serious problems now limiting forward speed and gross weight is the occurrence of unacceptably large blade torsional oscillations due to the periodic stalling and unstalling of each blade on the retreating side of the rotor disk (Ref. 1). Since the problem does not impact directly on either the thrust-producing capability or power requirements of the rotor system, its resolution would result in significant performance gains.

Stall problems have also arisen at the other extreme of the flight envelope. The space shuttle orbiter, in having to operate over a wide range of aerodynamic environments, can undergo numerous potentially detrimental unsteady stall phenomena, as outlined in Reference 2.

Dynamic stall is involved in continuing problems in other areas as well of course. Notable examples are rotating stall in axial-flow compressors (Ref. 3) and stall flutter of propellers and compressor blading (Ref. 4).

The studies which formed the basis for this paper were motivated by the helicopter stall problem, as is reflected in what follows. However, there is a considerable degree of commonality among the various problems involving unsteady stall, so the developments presented here should have relevance to other areas as well.

Early experimental studies of unsteady stall, such as those reported in References 5, 6, and 7, were concerned primarily with the stall flutter problem. From this work, the stall flutter mechanism of negative damping, or moment variation to extract energy from the flow, was deduced. More recently extensive tests on two-dimensional airfoils sinusoidally pitching or plunging through stall were carried out (Ref. 8) which make evident the complexity of the unsteady stall process. Both lift overshoot, or lift in excess of the maximum static value, and unstable moment variation were found to be strong functions of frequency, amplitude, mean incidence and Mach number.

Typical results from Reference 8, shown in Figure 1, illustrate the complexity of the problem. Normal-force and moment coefficients are plotted versus instantaneous angle of attack, with the static variation superimposed, for three values of reduced frequency of oscillation k . The tests were conducted with two-dimensional flow at a Mach number of .4, using a 10% thick cambered airfoil pitching about the quarter chord point. Lift hysteresis is seen to increase somewhat by changing k from .062 to .185, but with k of .302, there is almost no hysteresis. Lift overshoot, on the other hand, is relatively constant at about 25% of the maximum static C_n for all three cases, although similar tests for a symmetric airfoil reported in Reference 8 showed a large increase in overshoot with increasing k . It should be noted, too, that increasing k increases the area of unstable moment variation (clockwise loops), but that the maximum nose-down moment occurs with $k = .185$.

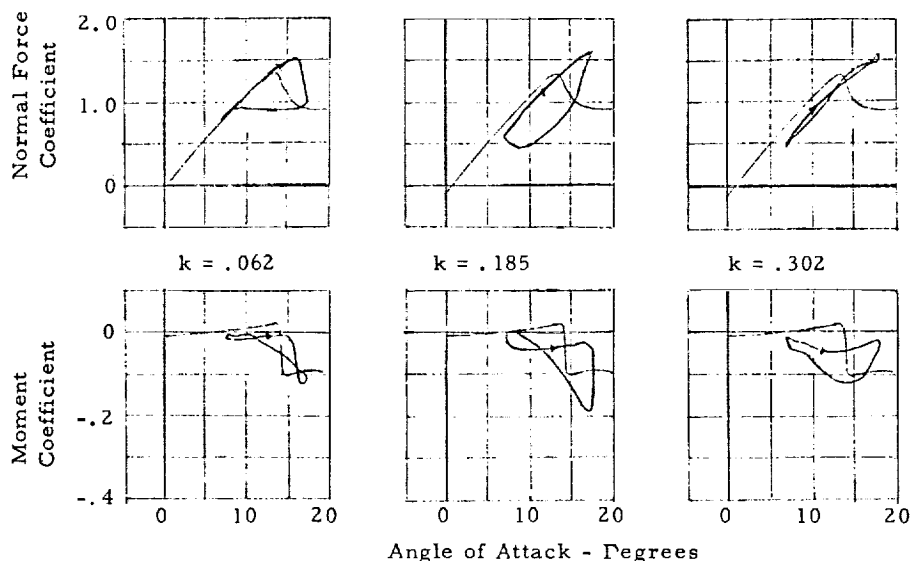


Figure 1. EFFECT OF FREQUENCY ON LOADING DURING SINUSOIDAL PITCHING (FROM REF. 8)

Other tests, of more limited scope but employing specialized instrumentation and flow visualization techniques, have revealed a number of important aspects of the problem. The formation of a leading-edge bubble, normally associated with airfoils subject to leading-edge stall, was detected in tests on model rotor blades (Refs. 9 and 10). Details of the stall onset process during leading edge stall, wherein a region of highly rotational flow forms at the leading edge and grows progressively from the leading to the trailing edge, was described in Reference 1 and was later observed in tests on a model rotor blade (Ref. 11) and on a two-dimensional airfoil (Ref. 12). Results from Reference 12 are shown in Figure 2, where upper-surface chordwise pressure distributions are plotted for several successive instants during stall onset for a NACA 0012 airfoil pitching at a reduced frequency of .1 with a mean incidence of 15 degrees and an amplitude of 14 degrees. The formation and growth of the trapped-air region are clearly marked by the secondary suction peak which progresses downstream with increasing angle of attack.

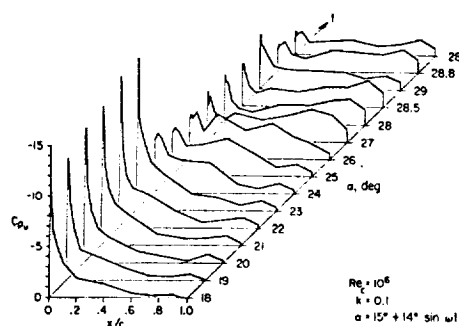


Figure 2. UPPER-SURFACE PRESSURE DISTRIBUTIONS AT STALL ONSET (FROM REF. 12)

The formation and growth of the trapped-air region are clearly marked by the secondary suction peak which progresses downstream with increasing angle of attack.

Analytical studies of various aspects of the stall problem as it relates to helicopter rotor blades have been carried out. Patay (Ref. 13) analyzed the unsteady boundary layer on a pitching Joukowski airfoil, and concluded that the flow in the boundary layer is essentially quasi-steady for dimensionless pitch rate $\dot{\theta} b/U$ as large as .05. Analyses of the unsteady laminar boundary layer on a rotating blade (Ref. 10) similarly showed that the chordwise pressure gradient dominates over both unsteady and rotational effects. The unsteady load on an oscillating stalled airfoil, for prescribed separation point location, was derived by Woods (Ref. 14), using classical unsteady thin-airfoil theory as a basis.

A number of analyses of unsteady stall of two-dimensional airfoils and rotors have been performed with viscous effects taken into account empirically. Ham (Ref. 15) analyzed a two-dimensional model consisting of discrete vortices shed from both the leading and trailing edges. Ericsson and Reding (Ref. 16) employed a quasi-steady approach which uses measured static airfoil characteristics. Carta and Niebanck (Ref. 17) utilized data from tests of two-dimensional oscillating airfoils and energy considerations to analyze stall flutter of a rotor blade. Rotor control loads due to stall are predicted by Tarzanin (Ref. 18) using an empirical model, again derived from data taken on oscillating airfoils, from which instantaneous loading during stall is computed. These methods generally yield good correlations with test data. A representative example is shown in Figure 3, where results obtained by Ham are compared with measured variations with time of lift and moment coefficients at stall onset.

While much insight regarding the unsteady stall process has been gained from both the experimental and the theoretical studies described above, the basic mechanisms for most important aspects of the problem have remained undefined. For that reason, a major portion of this paper has been devoted to a recently developed theory and its applications, which, it is felt, provides a better understanding of dynamic stall and the various factors contributing to its impact on specific systems. The theory, presented in Section 3, various details of which can be found in References 19, 20, and 21, was derived on the premise that analytic accounting of viscous effects and viscous-inviscid flow interactions is necessary to obtain an understanding of the underlying mechanisms of the stall problem. In taking this approach, a number of decisions were required concerning which flow elements must be regarded as essential to the stall process and what approximations could reasonably be employed in modeling those elements and their interactions. These aspects of the problem are discussed in the next section.

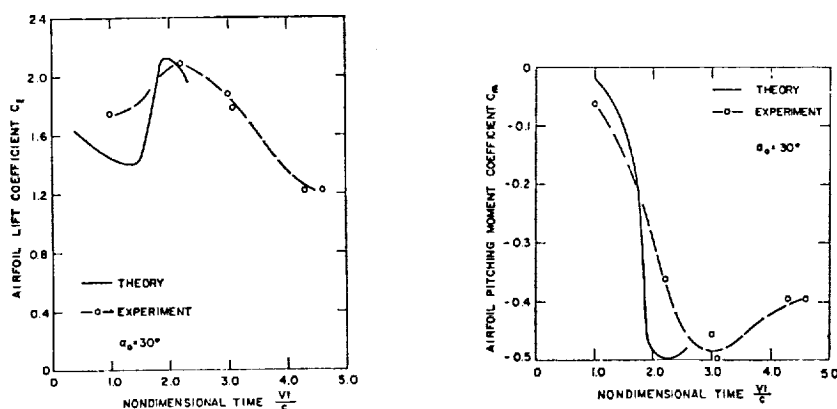


Figure 3. COMPARISON OF PREDICTED AND MEASURED LOADING DURING SUDDEN STALL (FROM REF. 15)

2. PROBLEMS IN MODELLING DYNAMIC STALL

Stall Mechanisms and Flow Elements

Even under steady conditions, airfoil stall is a complex phenomenon, with the loading dependent on many parameters, including Reynolds number, Mach number, leading-edge radius and thickness. The three basic mechanisms of stall in two dimensions, as first identified specifically by McCullough and Gault (Ref. 22) will be reviewed at this point to facilitate the delineation of the flow elements for the more general problem.

Trailing-edge stall is the most easily identified of the three types, being due to the separation of the turbulent boundary layer near the trailing edge. Increasing incidence moves the point of separation progressively forward along the airfoil, resulting in a gradual decrease in lift and increase in drag, as indicated in Figure 4a. This type of stall generally occurs on relatively thick airfoils at high Reynolds numbers.

Leading-edge stall is related to the formation of a small separation bubble near the leading edge. At a fairly low incidence, laminar separation occurs near the point of minimum pressure at the leading edge. The flow reattaches a short distance downstream of the separation point because of transition from laminar to turbulent flow in the free shear layer with subsequent turbulent mixing and reattachment. As the angle of attack increases, the bubble moves closer to the leading edge, grows slightly shorter and somewhat thicker. The bubble has almost no effect on integrated loads, because it is never more than a few percent of the chord in length. At some angle of attack, the bubble bursts and the flow separates from the entire upper surface of the airfoil, resulting in a sudden loss in lift, as indicated in Figure 4b. The precise reason for the bursting of the laminar bubble has been the subject of considerable controversy. There have been correlations attempted with bubble length and with boundary-layer momentum thickness at the point of laminar separation, with little success. There is a strong indication, though, that there is some maximum amount of pressure recovery which can occur in the turbulent mixing zone and still allow reattachment, and at some incidence the required recovery exceeds this maximum, causing sudden separation. Excellent reviews of the various theories and evidence related to leading-edge stall are given in References 23 and 24.

Thin-airfoil stall, which occurs at relatively low Reynolds numbers on thin airfoils, is characterized by the appearance of a laminar bubble springing from the leading edge at a relatively low incidence. Unlike the bubble formed prior to leading-edge stall, its point of separation remains fixed with increasing incidence while the bubble grows progressively larger. The processes of bubble formation and reattachment are not well understood (Ref. 23). The resulting lift curve is as sketched in Figure 4c. Because of the uncertainty as to precise mechanism of thin-airfoil stall and its relatively infrequent occurrence, the theory described in Section 3 does not include a model of the thin-airfoil stall mechanism. Elements necessary to account for both leading-edge and trailing-edge stall have been represented, however.

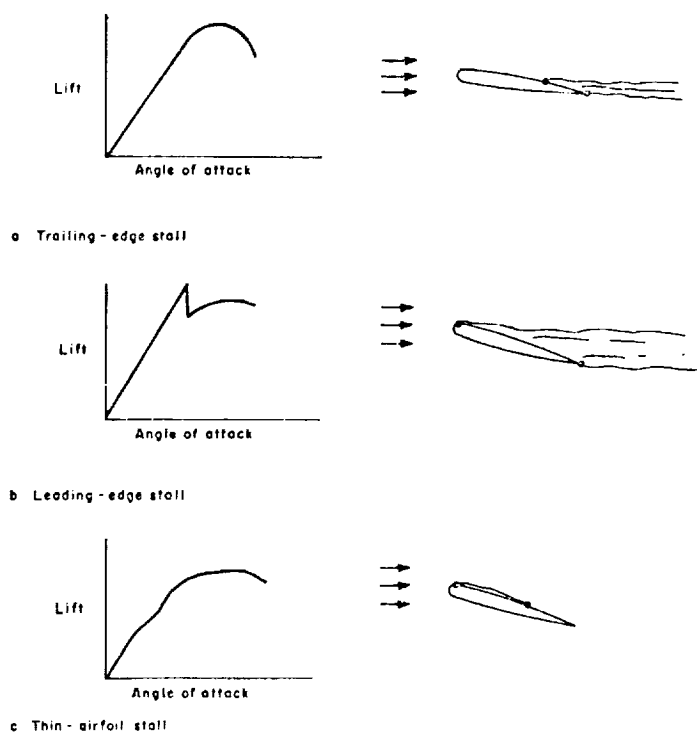


Figure 4. THE THREE TYPES OF AIRFOIL STALL

The primary flow elements of unsteady leading-edge or trailing-edge stall of a two-dimensional airfoil can be specifically identified, then, as indicated in Figure 5. When the flow is attached (Figure 5a), the flow elements are: (1) a laminar boundary layer extending from the stagnation point over the leading edge; (2) a leading-edge separation bubble (if separation occurs prior to transition); (3) a turbulent boundary layer from the reattachment point of the leading-edge bubble (or the transition point) to the trailing edge; and (4) a potential flow over the airfoil, including the effects of a vortical wake generated by the variation in time of the circulation about the airfoil. If the airfoil undergoes leading-edge stall (Figure 5b) and one regards the flow in the trapped-air region as essentially quasi-steady,* the flow elements are: (1) a laminar boundary layer to the point of separation; (2) a laminar constant-pressure free shear layer to the point of transition; (3) a turbulent constant-pressure free shear layer; (4) a turbulent pressure-recovery region; and (5) a potential flow over the airfoil and external to the trapped-air region, again including a vortical wake. Similarly, if trailing-edge stall occurs (Figure 5c), the flow elements are: (1) the laminar boundary layer; (2) the leading-edge bubble (if laminar separation occurs prior to transition); (3) the turbulent boundary layer; (4) a turbulent constant-pressure shear layer; (5) a turbulent pressure-recovery region; and (6) a potential flow with vortical wake.

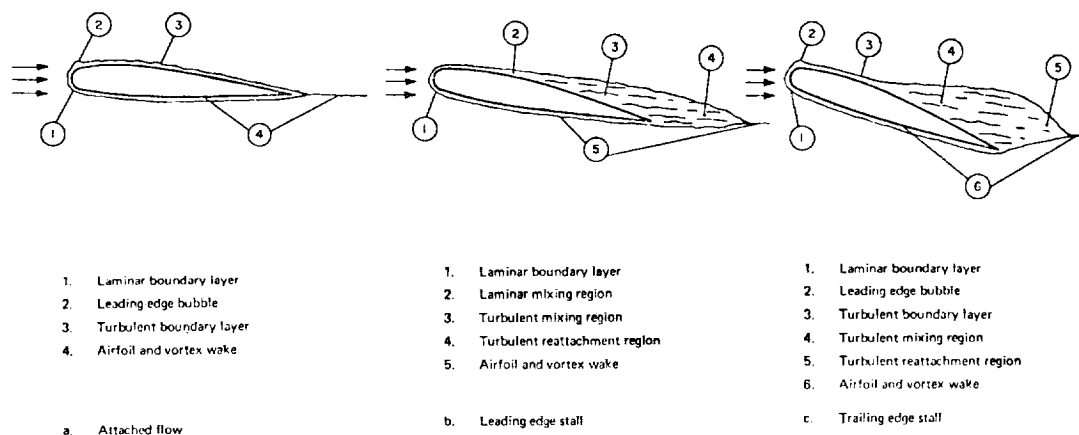


Figure 5. FLOW ELEMENTS

Unsteady Separation

As noted, for example, in Reference 25, vanishing wall shear does not necessarily imply boundary-layer separation in unsteady flow. A general separation criterion has been postulated in Reference 26, namely that the boundary-layer equations (but not necessarily the complete Navier-Stokes equations) are singular at the separation point for both steady and unsteady flows. Strong supporting evidence that this is a valid criterion is given in Reference 26, where a clearly defined singularity in the solution for the boundary layer on a moving wall is obtained in a region of negative wall shear.

What implications the definition of unsteady separation might have in the analysis of dynamic stall of a rotor blade were investigated by analyzing the laminar boundary layer upstream of the leading-edge bubble on a 10% thick symmetric airfoil (an NACA0012 section with small trailing-edge extension) using the unsteady finite-difference method described in Section 3. Chordal Reynolds number was 3 million and dimensionless pitch rate $\dot{\theta}_p b/U$ was .025. Results are shown in Figure 6, in which are plotted the external flow magnitude u_e , displacement thickness δ^* and wall shear as a function of distance along the airfoil surface from the stagnation point. The iteration on wall shear used in the finite-difference scheme diverged, apparently marking a singularity in the solution, at a streamwise mesh point .003 b upstream

*This would appear to be a reasonable assumption, since as will be discussed subsequently, the flow in the boundary layers is quasi-steady. However, as noted in Section 4, certain discrepancies between theory and experiment can be attributed to that assumption.

of the point of vanishing wall shear (estimated by extrapolation), which is clearly an insignificant distance in the determination of integrated load. At least in the case of leading-edge stall, then, definition of the unsteady separation point is not a critical problem.

The validity of the Sears-Telionis definition in unsteady turbulent boundary layers, of relevance to analysis of trailing-edge stall, is not immediately evident although it is asserted in Reference 26 that the extension is permissible. In any case, it would appear that this need not be of concern, since unsteady effects in the turbulent boundary layer were found to be relatively small for pitch rates normally experienced by rotor blades. Figure 7 compared analyses of the boundary layer downstream of the leading-edge bubble, again for $\dot{\theta}_{pb}/U = .025$ and a Reynolds number of 3×10^6 , one using the full unsteady boundary-layer equations (quasi-steady eddy viscosity) and the other with time derivatives dropped from both the boundary-layer equations and the expression for the imposed pressure distribution. The point of vanishing wall shear with quasi-steady flow assumed is seen to be only about 3.5% of the chord upstream of the point obtained using the complete equations. While one cannot conclude definitely that if unsteady effects are small, the separation point is close to the point of vanishing wall shear, that is the case for the laminar boundary layer, as indicated in Figure 6. For lack of both an alternative and evidence to the contrary, then, it must be assumed at present that the steady-flow definition of separation is applicable in the analysis of trailing-edge stall.

Stall Onset and Unstall Processes

In the case of trailing-edge stall, the stall onset and unstall processes are clearly defined by the movement of the separation point of the turbulent boundary layer. The situation during leading-edge stall is more complex, however.

After the leading-edge bubble bursts, the trapped-air region immediately begins to form, growing progressively from the leading edge to the trailing edge as fluid is garnered from the free stream by the actions of viscous shear and pressure gradients. The data in References 11 and 12 indicate that the rate of growth of the region is considerably less than the free-stream speed (roughly .1 U to .3 U). The following arguments can be made to the effect that the growth rate must, in fact, be of the order of the free-stream component normal to the airfoil chordline.

Let it be assumed that the assimilation of fluid mass takes place primarily at the downstream end of the trapped-air region, and that the fluid is trapped in the funnel-shaped region subtending an angle β , as sketched below (lengths and velocities shown are approximate, assuming angle of attack α is small). Let f be the

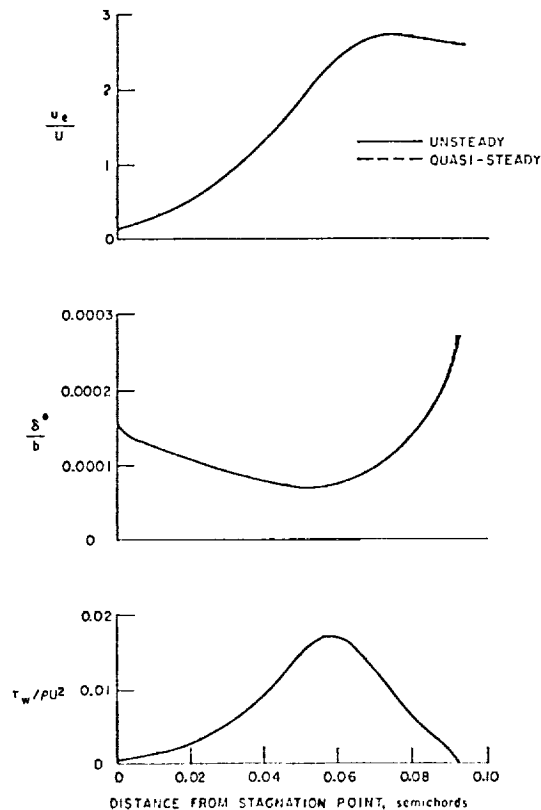


Figure 6. RESULTS OF LAMINAR BOUNDARY LAYER ANALYSIS

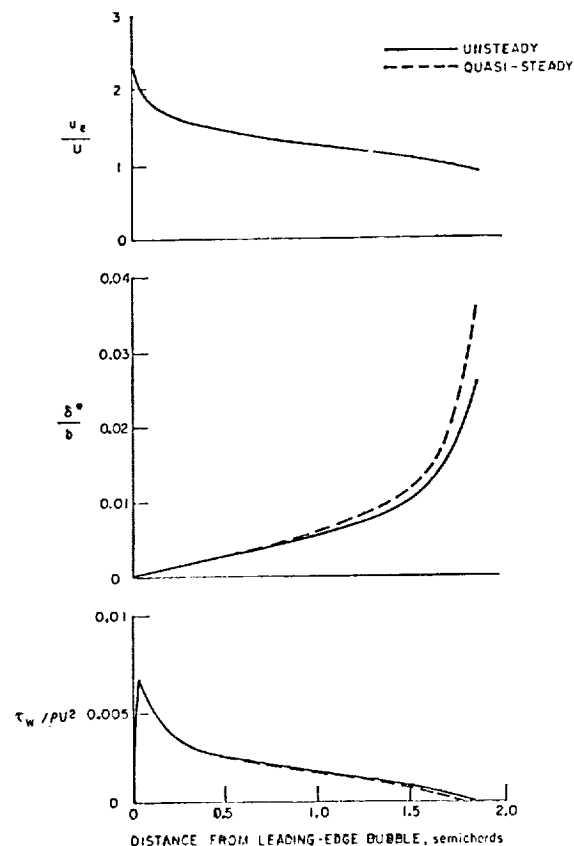


Figure 7. COMPARISON OF RESULTS OF TURBULENT BOUNDARY LAYER ANALYSES

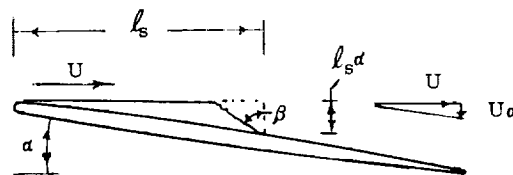
fraction of fluid entering the funnel which ultimately becomes part of the trapped-air region. Then the rate of increase of the mass of captured air is given approximately by

$$\dot{m} = f [\rho (\ell_s \alpha \tan \beta) (U \alpha)]$$

But \dot{m} is proportional to the rate of increase of area; $\dot{m} \approx \rho \ell_s \dot{\ell}_s$. Equating the two rates, it follows that

$$\dot{\ell}_s \approx (f \tan \beta) U \alpha$$

Thus, if $f \tan \beta$ is a number of order one (i.e., if most of the fluid is indeed trapped at the downstream end), ℓ_s is of the order of $U \alpha$.



The mechanism for initiation of un stall of an airfoil which has undergone leading-edge stall is presently unclear. In lieu of a direct means of determining when un stall occurs, the following procedure can be employed, if analysis is by forward integration in time. Suppose that at time t the airfoil is stalled. If, in the interval from t to $t + \Delta t$, the un stall process had begun, the portion of the trapped-air region near the leading edge would presumably have been washed away by the free stream, and a leading-edge bubble would have formed. It is only necessary, then, to postulate that that sequence of events had occurred and to analyze the leading-edge bubble. If the bubble bursts, then un stall could not have taken place, and the analysis continues with the airfoil remaining stalled. Otherwise, the un stall process is initiated. That process, during which the free stream recaptures the trapped fluid, must be similar to that of stall onset, so it would seem reasonable to assume that the wash-off rate is also of the order of the free-stream component normal to the chordline.

Other Factors

A number of other effects can play a significant role in the unsteady stall process under certain circumstances. For example, the amount of lift overshoot and hysteresis during sinusoidal pitching of an airfoil is a strong function of Mach number (Ref. 8). Compressibility effects can also cause periodic high-frequency stall and un stall of the airfoils at high subsonic Mach number and fixed incidence (Ref. 27). Three-dimensional effects are necessarily important in the stall of low-aspect-ratio wings and compressor blades. On the other hand, it was found that spanwise-flow effects were relatively small compared with chordwise pressure gradients on a helicopter rotor blade (Ref. 10). Separation from fuselages and similar bodies can result in complex unsteady phenomena such as periodic vortex shedding (Ref. 28), or randomly occurring asymmetric yawing moments (Ref. 29). Clearly, taking these and similar effects into account analytically could prove to be a formidable undertaking.

3. ANALYTICAL REPRESENTATION OF FLOW ELEMENTS

General Approach - Assumptions and Limitations

The basic objective of the analysis described in what follows was to construct a workable analytic model for unsteady airfoil stall, particularly as it relates to helicopter rotor blades, by representing each of the individual flow elements identified previously and consistently accounting for their interactions. Consideration has been limited to two-dimensional incompressible flow. Empirical relations were avoided throughout (except, of course, in the analysis of transition and turbulent flow, where their use to some degree is inevitable) even though employing them at certain junctures would have measurably improved quantitative agreement with test results, in order to extract as much information as possible regarding the role played by each flow element in the stall process.

In the formulation, the inviscid flow determination was regarded as a mixed boundary-value problem, with flow tangency required where the flow is attached and pressure specified in the separation region. The model for the trapped-air region provides the pressure distribution to be imposed. Taking this approach avoids the need for a direct accounting of displacement of the inviscid flow by the viscous flow. The only direct iteration between viscous and inviscid-flow solutions then required is one which locates the separation point.

Potential Flow

Given the airfoil section characteristics and motions, together with the distribution of pressure in the dead-air region if the airfoil is stalled, the flow and pressure over the airfoil must be determined in order to compute the integrated load and analyze the boundary layer. The problem is formulated as follows.

Consider an airfoil of infinite span and chord $2b$ subjected to a uniform, incompressible free stream of magnitude $U(t)$. Let $\theta_p(t)$ and $\dot{h}(t)$ denote the pitch angle and plunging rate of the airfoil, as shown in Figure 8. Further, let camber and thickness distributions $C(x)$ and $T(x)$, respectively, be defined by

$$C(x) = \frac{1}{2} \left[Y_U(x) + Y_L(x) \right]$$

$$T(x) = \frac{1}{2} \left[Y_U(x) - Y_L(x) \right]$$

where Y_U and Y_L are the ordinates of the upper and lower airfoil surfaces, respectively, measured from the chord line.

Only the problem of a stalled airfoil need be considered, because the solution for attached flow is readily recovered as a special case. The coordinates of the separation and reattachment points and the prescribed pressure between those points are denoted x_s , x_R and p_d , respectively.

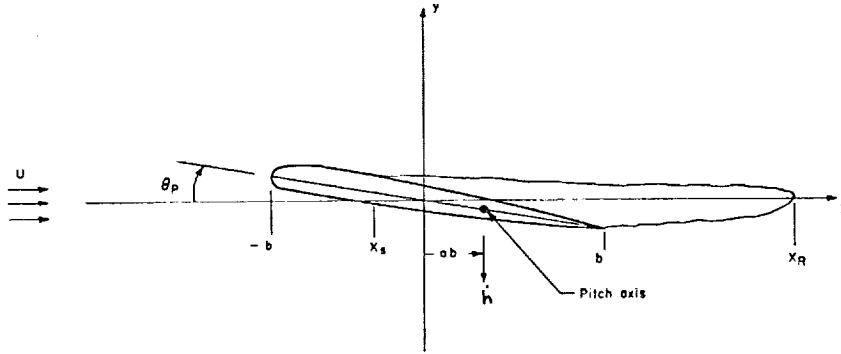


Figure 8. COORDINATE SYSTEM FOR POTENTIAL FLOW

In what follows, a perturbation velocity potential is derived by paralleling the approach taken by Lighthill (Ref. 30) for the problem of steady, attached flow, in order to obtain a solution which is uniformly valid to second order in the vicinity of the leading edge. The first step requires the derivation of a linearized solution.

Thus, let $u(x, y, t)$ and $v(x, y, t)$ denote components of the flow perturbation in the x and y directions, respectively, and let $p(x, y, t)$ denote the pressure. To first order, the boundary conditions which must be satisfied, for $x_R > b$, are then given by:

$$v(x, 0^\pm, t) = \pm UT' - w, \quad -b \leq x \leq x_s;$$

$$v(x, 0^\pm, t) = -UT' - w, \quad x_s \leq x \leq b;$$

$$p(x, 0^\pm, t) = p_d(x, t), \quad x_s \leq x \leq b;$$

$$p(x, 0^\pm, t) = p_d(x, t), \quad b \leq x \leq x_R.$$

where

$$w = U(\theta_p - C') + \dot{h} + (x - ab)\dot{\theta}_p$$

and similarly for the case with $x_R \leq b$.

The (+) and (-) signs affixed to the zero arguments designate the sign of y in the limit $y \rightarrow 0$. It is further required that the flow be continuous at the trailing edge (the Kutta condition) and at the separation point.

Assuming the flow is irrotational, a perturbation velocity potential ϕ can be formulated by distributing source and vortex singularities on the x -axis:

$$\phi = -\frac{1}{2\pi} \int_{-b}^{x_0} \left[\gamma(\xi, t) \tan^{-1} \left(\frac{y}{x - \xi} \right) - \sigma_0(\xi, t) \ln \sqrt{(x - \xi)^2 + y^2} \right] d\xi$$

where x_0 marks the location of the starting vortex. It is convenient to separate out thickness effects. Thus, let

$$\begin{aligned}\sigma_0(x, t) &= 2UT', \quad -b \leq x \leq x_s \\ &= 2UT' + \sigma(x, t), \quad x_s \leq x \leq b; \\ &= \sigma(x, t), \quad b < x \leq x_R \\ &= 0, \quad x_R < x \leq x_0.\end{aligned}$$

Also, the vortex strength for $x \geq b$ is known in terms of the strength on the airfoil, through conservation of circulation:

$$\gamma(b, t) = -\frac{1}{U} \frac{d}{dt} \int_{-b}^b \gamma(x, t) dx \quad (1)$$

and the vorticity downstream of the trailing edge is convected at the instantaneous free-stream speed (to first order), retaining the strength it had upon formation at the trailing edge, as prescribed by Eq. (1).

With the potential formulated in this way, the two unknown functions are the vortex strength γ on the interval $(-b, b)$ and the source strength σ over the interval (x_s, x_R) . The boundary conditions, written in terms of these two functions, are found to be (for $x_R > b$):

$$\frac{1}{\pi} \int_{-b}^b \frac{\gamma(\xi, t) d\xi}{x - \xi} = 2w - \frac{1}{\pi} \int_b^{x_0} \frac{\gamma_w(\xi, t) d\xi}{x - \xi}, \quad -b \leq x \leq x_s; \quad (2)$$

$$\sigma(x, t) + \frac{1}{\pi} \int_{-b}^b \frac{\gamma(\xi, t) d\xi}{x - \xi} = 2w - \frac{1}{\pi} \int_b^{x_0} \frac{\gamma_w(\xi, t) d\xi}{x - \xi}, \quad x_s \leq x \leq b; \quad (3)$$

$$\begin{aligned}\gamma(x, t) + \frac{1}{\pi} \int_{x_s}^{x_R} \frac{\sigma(\xi, t) d\xi}{x - \xi} &= \frac{2(p_\infty - p_d)}{\rho U} - \frac{2U}{\pi} \int_{-b}^b \frac{T'(\xi) d\xi}{x - \xi} \\ &- \frac{1}{U} \frac{\partial}{\partial t} \left\{ \int_{-b}^x \gamma(\xi, t) d\xi + \frac{1}{\pi} \int_{x_s}^{x_R} \sigma(\xi, t) \ln|x - \xi| d\xi \right. \\ &\quad \left. + 2 \frac{U}{\pi} \int_{-b}^b T'(\xi) \ln|x - \xi| d\xi \right\}, \\ &x_s \leq x \leq b;\end{aligned} \quad (4)$$

$$\begin{aligned}
\frac{1}{\pi} \int_{x_s}^{x_R} \frac{\sigma(\xi, t) d\xi}{x - \xi} &= \frac{2(p_\infty - p_d)}{\rho U} - \frac{2U}{\pi} \int_{-b}^b \frac{T'(\xi) d\xi}{x - \xi} \\
&- \frac{1}{U} \frac{\partial}{\partial t} \left\{ \frac{1}{\pi} \int_{x_s}^{x_R} \sigma(\xi, t) \ln|x - \xi| d\xi \right. \\
&\left. + \frac{U}{\pi} \int_{-b}^b T'(\xi) \ln|x - \xi| d\xi \right\}, \quad b \leq x \leq x_R.
\end{aligned} \quad (5)$$

The Cauchy principal value is taken for the singular integrals. A subscript w has been affixed to γ for $x > b$ to indicate that it is known in terms of γ for $x < b$.

Equations (2) through (5) were solved by first casting γ in series form, with unknown coefficients, and taking σ (with a singular term subtracted) to vary linearly between prescribed points on the x -axis, the value of σ at each of those points being unknown. Equations (2) through (5) provided the relations needed to solve for the unknown coefficients and the values of σ .

This procedure required that the functional form of γ and σ , i.e., the locations and types of singularities, first be determined. For that purpose, an analytical solution was derived for the case of steady flow about a stalled flat plate with constant pressure in the dead-air region. The derivation is outlined in Appendix A.

The solution for steady flow, as given in Appendix A, shows, first, that if x_R is greater than b , γ has the same functional form as for attached flow, i.e., γ has a square-root singularity at the leading edge and is continuous at both $x = x_s$ and $x = b$. If x_R is less than b , however, γ has a square-root singularity on the downstream side of $x = x_R$. Furthermore, regardless of the value of x_R , σ is zero at $x = x_s$ and has a square-root singularity at $x = x_R$ (necessarily on the upstream side).

Thus, γ was taken to be of the form

$$\begin{aligned}
\frac{\gamma(x, t)}{U_0} &= A_0 \sqrt{\frac{b-x}{b+x}} + \sum_{n=1}^{N_\gamma} A_n \sin n\theta \\
&+ \frac{\pi b}{4U} \left(1 + \frac{x}{b}\right) \left(1 - \frac{3x}{b}\right) \left(A_0 + \frac{A_1}{2}\right) \\
&+ A_R \left(1 + \frac{3x_R}{b} - \frac{4x}{b}\right) \sqrt{\frac{b-x}{x-x_R}}
\end{aligned} \quad (6)$$

where $\cos \theta = x/b$, U_0 is a reference velocity and the coefficients A_0 through A_{N_γ} and A_R are functions of time. The term with the factor A_R is dropped if either $x_R \geq b$ or $x < x_R$. The factors involving x in the last two terms make Eq. (6) satisfy Eq. (1) identically, as can be verified by direct substitution.

The form of σ was defined by first dividing the interval (x_s, x_R) into N_σ segments with end points $x_{\sigma i}$ given by

$$x_{\sigma i} = \frac{1}{2} (x_R + x_s) - \frac{1}{2} (x_R - x_s) \cos \left[\frac{(i-1)\pi}{N_\sigma} \right]$$

$i = 1, 2, \dots, N_\sigma + 1;$

whereupon

$$\frac{\sigma(x, t)}{U_0} = B_0 \sqrt{\frac{x-x_s}{x_R-x}} + \frac{(x_{\sigma i+1} - x) B_i + (x - x_{\sigma i}) B_{i+1}}{x_{\sigma i+1} - x_{\sigma i}} \quad (7)$$

$$x_{\sigma i} \leq x \leq x_{\sigma i+1}$$

$$(B_1 = B_{N_\sigma+1} \equiv 0)$$

where the B_i 's are unknown functions of time.

The coefficient A_R in γ , which is one of the unknowns when $x_R < b$, is in fact proportional to B_0 . If Eqs. (6) and (7) are substituted in Eq. (3) and the limit $x \rightarrow x_R$ is taken, it is found that the result can only be finite at $x = x_R$ (which it clearly must be) if

$$A_R = \left(1 - \frac{x_R}{b}\right)^{-3/2} \left(\frac{x_R - x_s}{b}\right)^{1/2} B_0$$

Thus, there are just $N_\sigma + N_\gamma + 1$ quantities to be determined at a given instant to completely define the flow and loading on the airfoil.

A set of linear algebraic equations was derived, using Eqs. (2) through (5), to provide the relations needed to solve for the unknowns. Specifically, after substituting Eqs. (6) and (7) for γ and σ , respectively, the flow-tangency boundary condition (Eqs. (2) and (3)) was imposed at points x_{γ_n} , where

$$x_{\gamma_n} = b \cos \left[\frac{(n-1)\pi}{N_\gamma} \right], \quad n = 1, 2, \dots, N_\gamma + 1;$$

and the pressure boundary condition (Eqs. (4) and (5)) was imposed at points \bar{x}_{σ_n} , where

$$\bar{x}_{\sigma_n} = \frac{1}{2} (x_{\sigma_n} + x_{\sigma_{n+1}}), \quad n = 1, 2, \dots, N_\sigma.$$

In the development of the linear algebraic equations, a number of assumptions and approximations were required.

Derivatives with respect to time in Eqs. (2) through (5) were approximated by second-order finite differences. Given the value of, say, A_0 at times t , $t - \Delta t$ and $t - 2\Delta t$, the relation

$$\dot{A}_0(t) = \frac{3A_0(t) - 4A_0(t - \Delta t) + A_0(t - 2\Delta t)}{2\Delta t} + O((\Delta t)^2)$$

was utilized, and similarly for the other required time derivatives.

Thickness and camber distributions were represented by trigonometric series so the integrals in which those functions appear could be evaluated analytically. Specifically, T and C were written in the form

$$T = b \sin \theta \left[\frac{1}{2} (1 - \cos \theta) \frac{r_0}{b} + \sin \theta \sum_{n=1} t_n \sin n\theta \right]$$

$$C = b \sin \theta \sum_{n=1} c_n \sin n\theta$$

where $\cos \theta = x/b$ and r_0 is the leading-edge radius. It was found that, using 24 terms, these series approximated the actual offsets of conventional NACA sections to within one percent (about .1 percent of chord) over the whole chord.

The wake downwash integrals appearing on the right-hand side of Eqs. (2) and (3) were evaluated by first specifying that the value of γ_w be known at discrete points along the x -axis, with the points spaced at a distance corresponding to the time increment Δt used for integration in time. The strength at each point is obtained as follows. Numbering the wake points from 1 to N_w (N_w increases by one after each time step), with point 1 at the trailing edge and point N_w at $x = x_0$, then $\gamma_{w1}(t)$ is computed from Eq. (1), using a second-order finite-difference approximation for the time derivative, while $\gamma_{wn}(t) = \gamma_{wn-1}(t - \Delta t)$ for $n = 2, 3, \dots, N_w$. The vortex strength is assumed to vary linearly between the designated points at which γ_w is known.

While the linear solution provides a good approximation for integrated loading, the flow and pressure distribution are singular at the leading edge, and so cannot be used to analyze the boundary layer. This difficulty can be resolved, in a manner similar to that employed in Reference 30, by including second-order terms in the potential and formulating the expression for the fluid velocity at the airfoil surface in such a way as to make the solution uniformly valid.

The functions σ and γ can be regarded as the first terms in series of ascending order representing the exact solution of the boundary-value problem. Let σ_2 and γ_2 denote the second-order terms in those series. If the full nonlinear flow-tangency requirement is expanded out to second order, and terms of like order are grouped in the usual manner, then σ_2 and γ_2 are found to be governed by the

following expressions:

$$\sigma_2 = \frac{2U}{\pi} \frac{\partial}{\partial x} \int_{-b}^b \frac{T'(\xi) d\xi}{x - \xi}$$

$$\frac{1}{2\pi} \int_{-b}^{x_0} \frac{\gamma_2(\xi, t) d\xi}{x - \xi} = - \frac{\partial}{\partial x} (T\gamma)$$

These relations are strictly applicable only to the case of attached flow. A complete accounting of second-order terms for a stalled airfoil could not be justified, in light of approximations made in the analysis of the trapped-air region. For that case, the result has been made uniformly valid to first order.

Note that the equation for γ_2 is of precisely the same form as the one for γ for attached flow. Hence, the same relations used to solve for γ could be used to obtain γ_2 after computing γ .

The same basic procedure as the one developed by Lighthill for steady flow (Ref. 30) was followed in deriving the formula for the magnitude of the fluid velocity at the surface q . The x -component of q , denoted q_x , is of the order of free-stream speed U , while the y -component, q_y , is of first order in whatever expansion parameter one chooses to use. Thus

$$q = q_x \sqrt{1 + (q_y/q_x)^2} = q_x + \frac{1}{2} \frac{q_y^2}{U} + \text{higher order terms.} \quad (8)$$

while

$$q_x = U \cos \theta_p + \frac{1}{2} (\gamma + \gamma_2) + u_s + \frac{1}{2\pi} \int_{-b}^b \frac{(2UT' + \sigma_2) d\xi}{x - \xi} + UTT'' + \text{third-order terms.}$$

$$q_y = U \sin \theta_p - \frac{1}{2\pi} \int_{-b}^{x_0} \frac{\gamma d\xi}{x - \xi} + v_s + UT' + \text{second-order terms.}$$

where θ_p is pitch angle and u_s and v_s are contributions from the source distribution representing the dead-air region when the airfoil is stalled. If these expressions for q_x and q_y are substituted in Eq. (8), the expected term which is singular at the leading edge due to a factor $(b+x)^{-1/2}$ is obtained. However, there is also a second-order term which is singular due to a factor $(b+x)^{-1}$, namely $U[TT'' + \frac{1}{2}(T')^2]$ which is approximately equal to $-.25 U r_o / (b+x)$ near the leading edge. A uniformly valid approximation for q is obtained, using Lighthill's procedure, by subtracting off the singular part of the offending term and multiplying by the factor

$$\left(\frac{b+x}{b+x+r_o/2} \right)^{1/2}$$

which restores the complete expression to its original form, to second order, some distance from the leading edge, and makes the result finite at the leading edge. The complete expression for q , uniformly valid to second order, with attached flow, is then

$$q = \left(\frac{b+x}{b+x+r_o/2} \right)^{1/2} \left\{ U \cos \theta_p + \frac{1}{2} (\gamma + \gamma_2) + u_s + UTT'' + \frac{1}{2\pi} \int_{-b}^b \frac{(2UT' + \sigma_2) d\xi}{x - \xi} \right. \\ \left. + \frac{1}{2U} \left[U \sin \theta_p - \int_{-b}^{x_0} \frac{\gamma d\xi}{x - \xi} + v_s + UT' \right]^2 + \frac{U r_o}{4(b+x)} \right\}$$

The pressure coefficient on the airfoil is computed from

$$C_p = 1 - \left(\frac{q}{U} \right)^2 = \frac{1}{U^2} \frac{\partial}{\partial t} \phi(x, 0^+, t)$$

Boundary Layer

Because the relative importance of the individual elements of the boundary-layer flow as they affect dynamic stall could not be established in advance, the representation of the boundary layer was made as general as possible to ensure that the effects of all essential elements were taken into account.

The method of finite differences, rather than an integral method, was selected for the analysis of both laminar and turbulent boundary layers because accuracy and computer requirements are readily controlled and the simpler formulation allowed rapid initial check-out of computer coding. The Smith-Cebeci eddy-viscosity model (Ref. 31), which has given good results for a wide range of Reynolds numbers and various types of pressure distribution, was chosen to represent the turbulent shear.

The boundary-layer equations were cast in the following dimensionless form for the cases of both laminar and turbulent flow:

$$\frac{\partial q_s}{\partial t} + q_s \frac{\partial q_s}{\partial s} + q_\eta \frac{\partial q_s}{\partial \eta} = - \frac{\partial \bar{p}}{\partial s} + \frac{\partial}{\partial \eta} \left(\bar{\nu}_e \frac{\partial q_s}{\partial \eta} \right) \quad (9)$$

$$\frac{\partial q_s}{\partial s} + \frac{\partial q_\eta}{\partial \eta} = 0 \quad (10)$$

Physical quantities relate to the variables in the above equations as follows. The flow component parallel to the surface is $U_o q_s$, the flow component normal to the surface is $U_o q_\eta / \sqrt{Re_b}$, where Re_b is Reynolds number based on semichord, time is bt/U_o , distance along the surface is bs , distance normal to the surface is $b\eta / \sqrt{Re_b}$ and pressure is $\rho U_o^2 \bar{p}$. For laminar flow, $\bar{\nu}_e = 1$ and for turbulent flow

$$\bar{\nu}_e = 1 + \frac{\epsilon}{\nu}$$

where ν is kinematic viscosity and ϵ is eddy viscosity. In terms of the variables defined above (see Ref. 31)

$$\frac{\epsilon}{\nu} = .16 \eta^2 \sqrt{Re_b} (1 - e^{-K})^2 \left| \frac{\partial q_s}{\partial \eta} \right| \equiv \bar{\epsilon}_i, \quad \eta < \eta_o;$$

where

$$K = \frac{\eta}{26} (Re_b)^{1/4} \left[\left(\frac{\partial q_s}{\partial \eta} \right)_{\eta=0} + \frac{\eta}{\partial s} \bar{p} \right]^{1/2}$$

and

$$\frac{\epsilon}{\nu} = \frac{.0168 (q_e/U_o) \bar{\delta}^*}{\sqrt{Re_b} [1 + 5.5 (\eta/\bar{\delta})^6]} = \bar{\epsilon}_o, \quad \eta > \eta_o$$

where

$$\bar{\delta}^* = \int_0^\infty (1 - q_s U_o / q_e) d\eta$$

while $\bar{\delta}$ is the value of η at which $q_s = .995 q_e / U_o$ and η_o is the value of η at which $\bar{\epsilon}_i = \bar{\epsilon}_o$.

The method employs variable step size in both the s and η directions. The error in each finite-difference approximation is of the order of the square of the step size. The differences were formulated to allow computation of the flow at time t and streamwise coordinate s_{m+1} , given the flow at times $t - \Delta t$ and $t - 2\Delta t$ at all streamwise coordinates and the flow at streamwise coordinates s_m and s_{m-1} for time t .

The solution for the flow at s_{m+1} is obtained by iteration. For the first iteration, the difference equations are linearized by employing extrapolation formulas for q_s , q_η , $\bar{\nu}_e$ and $\partial \bar{\nu}_e / \partial \eta$ in nonlinear terms. For the second and succeeding iterations, the values computed in the previous iteration are employed in place of the extrapolations.

Substitution of the finite-difference approximations in Eq. (9) yields a set of linear algebraic equations of the form

$$\tilde{A}_n q_{s_{m+1}, n-1} + \tilde{B}_n q_{s_{m+1}, n} + \tilde{C}_n q_{s_{m+1}, n+1} + \tilde{D}_n q_{s_{m+1}, n+2} = \tilde{F}_n \quad (11)$$

$$n = 2, 3, \dots, N_\eta - 1$$

where the coefficients \tilde{A}_n through \tilde{D}_n and \tilde{F}_n only involve flow quantities computed at s_m and s_{m-1} at time t and at s_{m+1} at previous time steps. After setting $q_{s_{m+1}}$ equal to zero and q_{s_{m+1}, N_η} and $q_{s_{m+1}, N_\eta+1}$ equal to $q_{e_{m+1}} / U_o$, Eqs. (11) are readily solved by successive elimination. Equation (10) can then be used to

compute q_η , from

$$q_\eta = - \int_0^\eta \left(\frac{\partial q_s}{\partial s} \right) d\eta$$

using a trapezoidal approximation.

The aforementioned iteration uses wall shear as the criterion for convergence, the allowable error being .1 percent. Some difficulty with convergence was encountered under extreme conditions. This problem was resolved by smoothing the eddy viscosity variation with η , as was done in Reference 21. After $\bar{\epsilon}$ is computed, its value is replaced by the mean of the values at three adjacent points.

The grid in the η direction is computed from a geometric progression. Given values of r_η and η_2 ($\eta_1 \equiv 0$), η_n is computed from

$$\eta_n = (1 + r_\eta) \eta_{n-1} - r_\eta \eta_{n-2}, \quad n = 3, 4, \dots, N_\eta + 1$$

At a given instant, the boundary layer thickness at the trailing edge is generally an order of magnitude larger than at the stagnation point. To accurately compute the flow at these extremes with a single grid in the η direction would require several hundred mesh points in that coordinate. About two hundred points are needed in the s -direction for a typical airfoil. Thus, an inordinate amount of computer storage would then be required, because the value of q_s at every mesh point for two time steps must be stored. Therefore, it was decided to make the η -scale variable. If, upon completion of the flow computation, the boundary-layer thickness $\bar{\delta}$ exceeds $\eta_{N_\eta-2}$, r_η is increased by a set amount, a new, expanded η -scale is computed and the flow quantities at the new mesh points are assigned by interpolation. The variation of the interpolated quantities is smoothed by three-point averaging, and computations proceed as before. The value of r_η is stored with the flow quantities so the boundary-layer profile can be reconstructed when needed. It should be noted that the value of η_2 is not changed when the η -scale is expanded. This is necessary to avoid numerical instability. Using the variable η -scale, only about 75 points are needed in the η -direction.

The computation is initiated at each instant using the Hiemenz stagnation-point profile (Ref. 32). The turbulent boundary layer downstream of reattachment of a leading-edge bubble is started from an equilibrium profile with a small but finite shear, taken from Reference 33, matching the computed displacement thickness with that of the equilibrium profile.

In the analysis of the laminar boundary layer, the solution at each s_m is used to determine whether transition occurs, accounting for the effects of free-stream turbulence and pressure gradient. The following formula, which is a modification of a result given in Reference 34, is used to compute transition Reynolds number $Re_{\delta_{tr}}$:

$$3.6 \left(\frac{u'}{q_e} \right)^2 Re_{\delta_{tr}}^2 + f_p(\Lambda) Re_{\delta_{tr}} - 9860 = 0 \quad (12)$$

where u' is the root-mean-square fluctuation of the free stream due to turbulence, Λ is the Kármán-Pohlhausen pressure-gradient parameter, $\Lambda = -(\delta^2 \partial p / \partial x) / \mu q_e$, and $Re_{\delta_{tr}}$ is the maximum Reynolds number, based on boundary layer thickness and local external flow, for which the flow remains laminar. The function $f_p(\Lambda)$, plotted in Figure 9, was derived from data given in Reference 32 pertaining to the effects of pressure gradient on transition, starting from the plot of $Re_{\delta_i}^*$ vs. Λ (Figure 17.3 of Ref. 32), where $Re_{\delta_i}^*$ is a Reynolds number based on displacement thickness at the point of instability. Using the Karman-Pohlhausen integral method and the plot of $Re_{\theta_{tr}} - Re_{\theta_i}$ vs. mean pressure gradient parameter \bar{K} (Figure 17.9 of Ref. 32), where $Re_{\theta_{tr}}$ and Re_{θ_i} are Reynolds numbers based on momentum thickness θ at the points of transition and instability, respectively, and \bar{K} is the integral average of $-(\theta^2 \partial p / \partial x) / \mu q_e$, $Re_{\delta_{tr}}$ was computed as a function of Λ and the curve of Figure 9 was constructed. The terms of Eq. (12) which account for free-stream turbulence (i.e., with $f_p = 1$) were taken directly from Reference 34. The form of the terms was derived there from arguments concerning the relation of viscous shear to transition. The relation agrees well with measured transition Reynolds number for a flat plate. Similar arguments were used in Reference 34 to derive the effects of pressure gradient on transition. The result is an equation of the same form as Eq. (12) but with f_p simply varying linearly with Λ . It was felt that the relation so obtained was not suitable for the problem at hand, in that it did not give good correlation with experiment and does not properly reflect the stabilizing influence of a favorable pressure gradient. The term accounting for effects of pressure gradient was therefore derived by the procedure previously described.

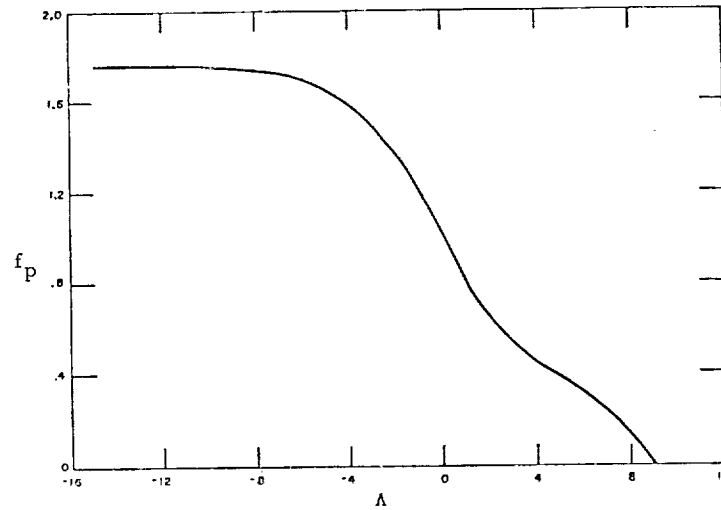


Figure 9. FUNCTION TO ACCOUNT FOR PRESSURE-GRADIENT EFFECT ON TRANSITION

Trapped-Air Region

As was noted previously, the region of trapped air which forms when the airfoil is stalled is assumed to consist, in the most general case, of a laminar constant-pressure free shear layer, a turbulent, constant pressure mixing region downstream of transition, and downstream of the latter region, a turbulent reattachment, or pressure-recovery region. The representation of each of these, starting with the reattachment region, is outlined in what follows.

Reattachment region - In this part of the trapped-air region, the layer thickness shrinks to zero while the streamwise pressure gradient is positive. The separated shear layer may reattach onto the airfoil or attach onto the layer shed from the lower surface at a stagnation point in the wake. It is assumed that the flow has a wake-like behavior and that the equilibrium wall layer usually present in attached turbulent boundary layers can be ignored. The wall shear stress is also assumed negligible compared with the properly normalized rate of change of momentum thickness and the streamwise pressure gradient. These assumptions and the analytical model which will be employed here have been used by Todisco and Reeves (Ref. 35) and Hunter and Reeves (Ref. 36) to treat supersonic separated and reattaching turbulent flows.

For negligible wall stress and zero lateral pressure gradient normal to the dividing streamline the momentum integral and first moment of momentum equations are (Ref. 35)

$$H \frac{d\delta^*}{dx} + \delta^* \frac{dH}{dx} + (2H+1) \frac{\delta^*}{U_e} \frac{du_e}{dx} \approx 0$$

$$J \frac{d\delta^*}{dx} + \delta^* \frac{dJ}{dH} \frac{dH}{dx} + \frac{3J\delta^*}{U_e} \frac{du_e}{dx} = K_\theta H \bar{R}$$

Because $J = J(H)$, $\bar{R} = \bar{R}(H)$, and $K_\theta = K_\theta(H)$ are known profile functions obtained from a one-parameter family of equilibrium or self-similar solutions the dependent variables are the velocity profile shape parameter $H = \theta/\delta^*$, displacement thickness δ^* and the local inviscid velocity at the edge of the turbulent layer u_e . For supersonic separation and reattachment a third differential equation involving these three dependent variables is obtained by coupling the integral continuity equation with the Prandtl-Meyer relationship. This third equation completes the set. In the case of subsonic flow, the interaction of the separated flow with the outer inviscid stream is much more complicated because of the absence of a local relationship between turning angle and pressure. Rather than attempt a complete matching of the inviscid and viscous flows, approximate relationships between certain quantities appearing in the integral equations were obtained from the well developed theory of supersonic interactions, and the matching performed in terms of only a few parameters.

The momentum integral and first moment can be rearranged and combined to give the following explicit relations for the derivatives of displacement thickness and inviscid velocity:

$$d(\ln \delta^*) = \left[\frac{-3J + (2H+1) dJ/dH}{J(H-1)} \right] dH - \frac{(2H+1) K_\theta H \bar{R}}{J(H-1)} \frac{dx}{\delta^*}$$

$$d(\ln u_e) = - \left[\frac{H \frac{dJ}{dH} - J}{J(H-1)} \right] dH + \frac{K_\theta H^2 \bar{R}}{J(H-1)} \frac{dx}{\delta^*}$$

These equations are solved using the method of successive approximations. By first assuming that reattachment occurs over a sufficiently short streamwise distance (compared with the local displacement thickness), so the second term on the RHS of the first of these equations is negligible, one obtains

$$\delta^* / \delta_{b^*} = \exp \int_{H_b}^H f(H) dH$$

where

$$f(H) = \frac{-3J + (2H+1) dJ/dH}{J(H-1)}$$

and subscript b denotes conditions at the beginning of the reattachment pressure rise. Substituting this first approximation for δ^* into the differential equations for δ^* and u_e and integrating gives

$$\begin{aligned} \ln(\delta^* / \delta_{b^*}) &= \int_{H_b}^H f(H) dH \\ - \exp \left[\int_{H_b}^{H_R} f(H) dH \right] &\int_{H_b}^H \frac{(2H+1) K_\theta H \bar{R}}{J(H-1) \exp \int_{H_b}^H f(H') dH'} \frac{d \left(\frac{x - x_R}{\delta_{R^*}} \right)}{d(H/H_R)} \frac{dH}{H_R} \end{aligned} \quad (13)$$

and

$$\begin{aligned} \ln(u_e / u_{eb}) &= - \int_{H_b}^H \left[\frac{H dJ/dH - J}{J(H-1)} \right] dH \\ + \exp \left[\int_{H_b}^{H_R} f(H) dH \right] &\int_{H_b}^H \frac{K_\theta H^2 \bar{R}}{J(H-1) \exp \int_{H_b}^H f(H') dH'} \frac{d \left(\frac{x - x_R}{\delta_{R^*}} \right)}{d(H/H_R)} \frac{dH}{H_R} \end{aligned} \quad (14)$$

where subscript R denotes conditions at the reattachment point (or wake stagnation point if closure occurs in the wake). It is now assumed that the streamwise rate of change of the turbulent shear layer velocity profile (or rather the inverse, $d(x/\delta_{R^*})/dH$) is a universal function for all incompressible turbulent reattachment processes. This function was evaluated from several solutions of supersonic reattaching shear layers with the results shown in Figure 10. The variables x and δ_{i^*} are the "stretched" values after having been transformed by a modified Stewartson compressibility transformation. Three curves for $(x - x_R)/\delta_{i^*R}$ versus H/H_R for Mach number M'_∞ varying between 1.3 and 2.2 are given. It is evident that the curves collapse into a single curve as the Mach number is reduced. Thus, it is assumed that the curve shown for $M'_\infty = 1.3$ defines the streamwise rate of change of the profile shape in all turbulent reattachment processes. Values of the derivative $d(x/\delta_{R^*})/d(H/H_R)$ obtained from this curve and values of the profile function obtained from equilibrium turbulent boundary layer solutions are given in Table I.

Figure 10 also shows the variation of $(x_b - x_R)/\delta_{i^*b}$ with H/H_R , that is, the reattachment length normalized by displacement thickness at the beginning of reattachment (only the curve for $M = 1.3$ is shown). This curve can be represented quite well by the parabola:

$$(x_R - x_b)/\delta_{b^*} = 10.5 \left[1 - (H_b/H_R)^2 \right] \quad (15)$$

Because H_b and δ_{b^*} are determined by the solution of the constant pressure mixing region this relationship can be used to find the length of the reattachment region without having to first compute the velocity and displacement thickness distributions through the reattachment region.

*When not employed as a subscript, b denotes airfoil semichord.

Table I. PROFILE FUNCTIONS FOR TURBULENT SEPARATED FLOWS^a

H/H_R	$d\left(\frac{x - x_R}{\delta_R^*}\right)/d\left(\frac{H}{H_R}\right)$	J/J_R	$d\left(\frac{J}{J_S}\right)/d\left(\frac{H}{H_S}\right)$	\bar{R}/\bar{R}_R	$\frac{\bar{R}H}{\bar{R}_R H_R}$
0	--	0	--	--	0
.1	83	.18	1.08	2.98	.298
.2	46	.28	.95	2.53	.506
.3	33	.37	.91	2.23	.669
.4	26	.46	.90	1.98	.792
.5	22	.54	.90	1.78	.890
.6	20	.62	.91	1.60	.960
.7	20	.70	.93	1.45	1.015
.8	20	.79	.96	1.30	1.04
.9	21	.89	1.00	1.15	1.035
1.0	23	1.0	1.04	1.00	1.00
1.1	25	1.12	1.11	.86	.946
1.2	29	1.24	1.18	.72	.864

^aNOTE: $H_R = H_S = .429$, $J_R = J_S = .654$, $\bar{R}_R = .463$, and $K_\theta = .05 - .0132 (H/H_R)$. Also, it is convenient to use the product $\bar{R}H$ as $H \rightarrow 0$ rather than \bar{R} because in this limit $\bar{R} \rightarrow \infty$ but $\bar{R}H \rightarrow 0$.

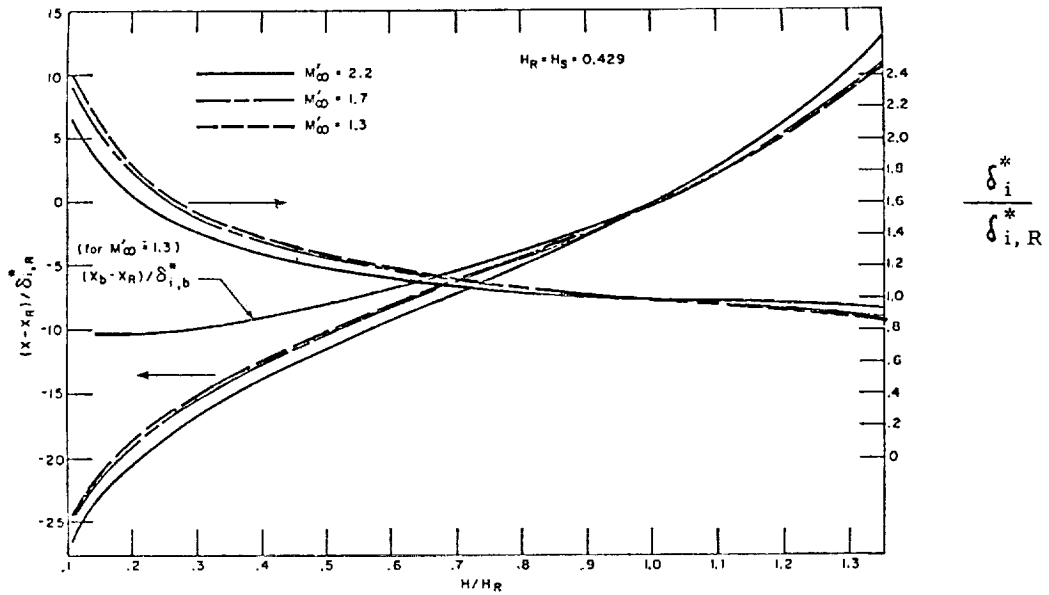


Figure 10. CORRELATIONS FOR TURBULENT REATTACHMENT

Turbulent mixing region - Since the pressure is constant in this region, the momentum integral and first moment equations reduce to the following:

$$H \frac{d\delta^*}{dx} + \delta^* \frac{dH}{dx} = 0$$

$$J \frac{d\delta^*}{dx} + \delta^* \frac{dJ}{dx} = K_\theta H \bar{R}$$

Now, let the subscript t denote conditions at the transition point in the shear layer. If the layer is turbulent at the separation point then $H_t = H_s$, $\delta_t^* = \delta_s^*$, etc.

The solution of the first of these equations is

$$\delta^* H = \delta_t^* H_t = \text{constant}$$

and substitution of the first equation into the second gives

$$\frac{\delta_t^* H_t}{H} \left(\frac{dJ}{dH} - \frac{J}{H} \right) \frac{dH}{dx} = K_\theta H \bar{R}$$

Rearranging this expression and integrating from the transition point (or separation point for trailing-edge stall) to the beginning of reattachment gives

$$\frac{x_b - x_t}{\delta_t^*} = J_s \frac{H_t}{H_s} \int_{H_t/H_s}^{H_b/H_s} \frac{1}{K_\theta \bar{R} H (H/H_s)} \left[\frac{d(J/J_s)}{d(H/H_s)} - \frac{(J/J_s)}{(H/H_s)} \right] d\left(\frac{H}{H_s}\right) \quad (20)$$

and from the solution $\delta^* H = \text{constant}$

$$\frac{\delta_b^*}{\delta_t^*} = \frac{(H_t/H_s)}{(H_b/H_s)}$$

At the transition point we assume that the velocity along the dividing streamline and the momentum thickness are continuous so that*

$$(\theta_t)_{\text{lam}} = (\theta_t)_{\text{turb}}$$

and

$$\left(\frac{H_t}{H_s}\right)_{\text{lam}} = \left(\frac{H_t}{H_s}\right)_{\text{turb}}$$

Consequently, since $H \equiv \theta / \delta^*$

$$(\delta_t^*)_{\text{turb}} = (\delta_t^*)_{\text{lam}} (H_s)_{\text{lam}} / (H_s)_{\text{turb}} = .58 (\delta_t^*)_{\text{lam}}$$

Because x_t , $(H_t/H_s)_{\text{lam}}$ and $(\delta_t^*)_{\text{lam}}$ are known from the solution of the laminar shear layer, the above expressions are sufficient to determine the length of turbulent mixing region and the displacement thickness at the beginning of reattachment in terms of the unknown profile shape parameter H_b at this point.

The laminar mixing region - For the laminar shear layer extending from the separation point to transition, the momentum integral and first moment equations are (for zero pressure gradient)

$$H \frac{d\delta^*}{dx} + \delta^* \frac{dH}{dx} = \left(\frac{\nu}{u_e \delta^*} \right) P$$

$$J \frac{d\delta^*}{dx} + \delta^* \frac{dJ}{dx} = \left(\frac{\nu}{u_e \delta^*} \right) R$$

where

$$P = \frac{\delta^*}{U_e} \left(\frac{\partial u}{\partial y} \right)_{y=0}, \quad R = \frac{2 \delta^*}{U_e^2} \int_0^{\delta} \left(\frac{\partial u}{\partial y} \right)^2 dy$$

Solution of this pair of equations has been given in Reference 37. The solution presented there was for the variation of the displacement thickness and dividing streamline velocity as functions of the nondimensional length scale downstream of separation $x^2/\theta_s^2 Re_x$. Since at a laminar separation point it can be assumed that $H_s = \theta_s / \delta_s^* = .25$, the above length scale can be cast into the form

$$Re_x / (Re \delta_s^*)^2 = .062 x^2 / \theta_s^2 Re_x$$

Also, H/H_s is a function of u^* (the ratio of the velocity along the dividing streamline to u_e), so that the solution given in Reference 37 can be used here with only slight modification. The variation of H/H_s and δ^* / δ_s^* with distance downstream of separation is shown in Figure 11. Here x is the distance downstream of the separation point.

*This procedure for finding the turbulent momentum thickness, displacement thickness and profile shape downstream of transition is analogous to the method used by Truckenbrodt for attached boundary layers (Ref. 32).

It is assumed that the length of the laminar shear layer is determined by von Doenhoff's criterion, namely that $(Re_x)_t = 50,000$.* Thus, $(H_t/H_s)_{lam}$ and $(\delta_t^*/\delta_s^*)_{lam}$ are known functions of $Re_{\delta_s^*}$, as indicated in Figure 11. The characteristic velocity in each of these Reynolds numbers is the local velocity at the separation point.

Pressure calculation procedure - Given the locations of the separation and reattachment points and the pressure at reattachment, it is required to compute the distribution of pressure between x_s and x_R . The basic problem is to determine H_b and x_b . With H_b known, the rise in pressure from x_b to x_R can be computed directly from Eq. (14). Since the pressure at x_R is specified and the pressure is constant from x_s to x_b , the pressure distribution is then completely determined.

The two relations used to determine x_b and H_b are Eqs. (15) and (16). Equation (16) relates $x_b - x_t$ (or $x_b - x_s$, in the case of trailing-edge stall) to H_b , while Eq. (15) relates $x_R - x_b$ to H_b . A simple iterative calculation is performed whereby successive values of H_b are assumed and x_b is computed from Eqs. (15) and (16). A solution is obtained when the two results for x_b agree within a prescribed amount.

Leading-Edge Bubble

In the analysis of the leading-edge bubble, it is assumed that the beginning of the reattachment region and the point of transition are coincident. The formulations developed for the viscous mixing and reattachment regions can then be employed, as follows.

From the curves of Figure 8, the conditions at transition, and hence at x_b , can be obtained, given δ^* and θ at separation from the boundary-layer analysis. Since x_b , which is assumed equal to x_t , is known from von Doenhoff's criterion $((x_t - x_s) q_{es}/\nu = 50,000)$, x_R can be computed directly from Eq. (15). Also, the pressure rise possible in the reattachment region can be obtained from Eq. (14).

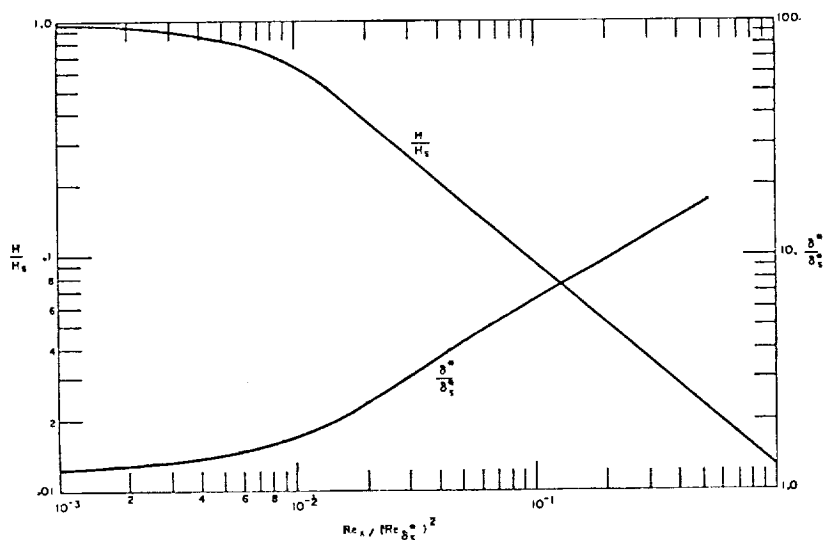


Figure 11. H AND δ^* VARIATIONS DOWNSTREAM OF SEPARATION FOR A LAMINAR SHEAR LAYER

It is assumed that the pressure rise across the bubble, from x_s to x_R , is not affected by the presence of the bubble. Given x_s and x_R , the potential-flow solution is then used to compute that increase in pressure. If the pressure rise computed from Eq. (14) exceeds the required pressure rise computed from the potential-flow solution, it is assumed that the mixing process accommodates to the lower required pressure rise and that the flow reattaches. If the required pressure rise exceeds the pressure rise computed from Eq. (14), it is assumed the leading-edge bubble has burst and the airfoil is undergoing leading-edge stall.

It should be noted that, although the above analysis was carried out independently, the key assumptions and basic procedures were, in fact, first derived by Horton (Ref. 39). The two approaches differ primarily in the details of the shear-layer analyses.

Computation Procedure

The procedure used in analyzing the interactions of the flow elements is indicated schematically in Figure 12. The computations are carried out by forward integration in time, starting from steady,

*Gault (Ref. 38) has performed a large number of experiments in which $(Re_x)_t$ ranged between 25,000 and 75,000 for over 80 percent of the data. Consequently, as Gault points out, a unique value for this transition Reynolds number is only a rough approximation and is influenced by the turbulence level, pressure gradient, etc.

attached flow. At each time step, when the flow is attached, prescribed airfoil motions are used to derive the potential flow. The flow external to the boundary layer is then computed. The boundary layer and leading-edge bubble are then analyzed to determine whether the leading-edge bubble has burst (leading-edge stall) or the turbulent boundary layer has separated (trailing-edge stall). If the flow remains attached, time is incremented, the foil motions are again prescribed and the procedure repeated.

If the airfoil stalls, the location of the separation point is assumed, the point of reattachment and pressure at reattachment are computed by a method to be described subsequently, the pressure in the dead-air region is computed and the potential-flow solution is derived from the prescribed airfoil motions and dead-air pressure distribution. The boundary layer is then analyzed and the computed separation point location is compared with the assumed location. If the assumed location differs by more than a prescribed amount from the computed one, a new estimate of the separation point location is made and the potential flow and boundary layer are again analyzed. When the assumed and computed separation point locations are in satisfactory agreement, time is incremented.

Except at the onset of leading-edge stall, the length of the trapped-air region when the airfoil is stalled is computed by deriving a bubble growth rate from the potential solution and integrating in time. The growth rate is computed as follows. The rate of increase of mass of the dead-air region is given, to first order, by

$$\dot{m} = \rho \int_{x_s}^{x_R} \sigma \, dx$$

The total mass of the dead-air region is roughly proportional to $\rho l_s \bar{Y}_{\max}$, where $l_s = x_R - x_s$ and \bar{Y}_{\max} is the maximum of $\bar{Y}(x)$,

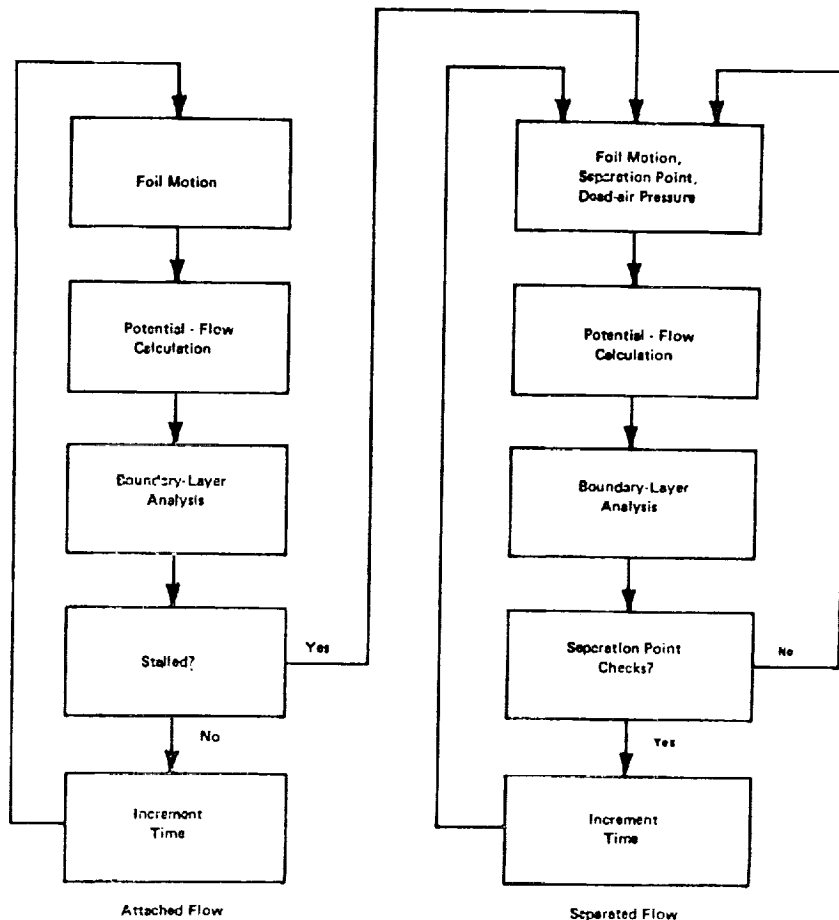


Figure 12. COMPUTATION PROCEDURE

where

$$\bar{Y}(x) = \int_0^x \frac{\sigma(\xi) d\xi}{U}$$

If added mass is all accountable as additional length, then

$$\frac{\dot{l}_s}{l_s} = \frac{\dot{m}}{m} = \frac{\int_{x_s}^{x_R} \sigma dx}{l_s \bar{Y}_{\max}}$$

The primary justification for computing x_R in this way is that it gives a closed trapped-air region (i. e., with zero net source strength) in the limit of steady separated flow.

As was noted previously, the growth rate of trapped-air region at the onset of leading-edge stall is estimated to be of the order of the free-stream component normal to the chordline. On that basis, a value for \dot{l}_s of .25 U at stall onset was selected, except where otherwise noted, for computational purposes. The same value was assigned to the rate at which the trapped-air region is washed off during unstall following leading-edge stall.

When the dead-air region terminates downstream of the trailing edge, the pressure at x_R is taken to be the free-stream pressure. If x_R is less than b, as occurs at the onset of leading-edge stall, the pressure at x_R is taken to be the pressure at that point if the airfoil were not stalled.

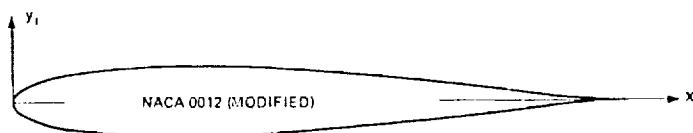
4. RESULTS FOR PRESCRIBED AIRFOIL MOTIONS

A series of calculations of the loading during unsteady stall due to transient and sinusoidal pitching about the quarter-chord were performed for the modified NACA 0012 airfoil section shown in Figure 13. The results reveal a number of interesting features of the stall process.

Transient Pitching Motions - Static Stall Characteristics

It was found that at a chordal Reynolds number of two million, only leading-edge stall is predicted to occur. Figure 14 shows the variations, at that Reynolds number, of pitch angle, normal-force and moment coefficients and length of the trapped-air region with time, as well as upper-surface pressure coefficient chordwise variations at three different times after stall onset, for a ramp variation of pitch angle. The underlying mechanisms of the dynamic stall process are evident from these results. The substantial lift overshoot seen in Figure 14 derives in part from a delay in bursting of the leading-edge bubble to beyond the static stall incidence, the effective camber due to pitch rate having reduced the pressure gradient in the vicinity of the leading edge. Carta, in Reference 40, postulated that this might be a contributing factor. Most of the overshoot comes after bubble burst, however, and, as can be seen from the pressure distributions, is the result of the very high loading induced on the aft portion of the airfoil by the presence upstream of the region of trapped, highly rotational fluid. Note that the large downstream suction peaks are just downstream of the instantaneous terminus of the trapped-air region. Because the high loading is on the aft portion of the airfoil, lift overshoot is necessarily accompanied by a large nose-down moment.

The variations of static normal-force and moment coefficient with angle of attack were obtained from a series of transient pitch calculations by parametrically varying the maximum pitch angle. The results are compared with measured coefficients, at a slightly higher Reynolds



x_1/c	Y_u/c
0	0
.0110	.0170
.0220	.0230
.0320	.0270
.0540	.0340
.0760	.0390
.1087	.0445
.1521	.0493
.2065	.0527
.2500	.0542
.3043	.0547
.3478	.0541
.4130	.0520

x_1/c	Y_u/c
.4562	.0499
.5000	.0472
.5434	.0439
.6086	.0383
.6521	.0343
.6955	.0300
.7607	.0230
.8042	.0181
.8477	.0127
.8911	.0070
.9346	.0011
1.000	.0011

$re/c = .0143$

Figure 13. AIRFOIL SECTION

number from Reference 8 in Figure 15. Agreement in the maximum static C_n is seen to be quite good, although the predicted stall incidence is considerably less than the measured value, due in part to the difference in slopes of the C_n curves below stall. Accounting for boundary-layer displacement effects would presumably improve the agreement in that respect.

One would expect that an airfoil which is subject to leading-edge stall at a certain Reynolds number would undergo trailing-edge stall at a much higher Reynolds number, since transition would then preclude formation of a leading-edge bubble. At intermediate Reynolds numbers, presumably either type of stall could occur. Calculations were performed to investigate the effect of varying Reynolds number on dynamic and static stall characteristics in this intermediate range of Reynolds numbers.

The loading resulting from transient pitching through stall was analyzed for chordal Reynolds numbers of 3 and 6 million, for comparison with the results obtained at a Reynolds number of 2 million. Pitch angle was again varied linearly with time up to a prescribed value and then held constant.

Increasing Reynolds number to 3 million caused a marked increase in the resistance to bursting of the leading-edge bubble. The airfoil does not undergo leading-edge stall for pitch angles as high as about 16 degrees, but does experience trailing-edge stall between about 12 and 16 degrees. At a steady-state pitch angle of 15.8 degrees, separation of the turbulent boundary layer has progressed upstream to near the quarter-chord point.

As the separation point of the turbulent boundary layer moves up the chord, the resistance of the leading-edge bubble to bursting continuously decreases, even though the circulation and loading on the airfoil are decreasing as well. The reason for this is that the separated region has relatively little effect on the flow in the immediate vicinity of the leading edge, even though it reduces the loading over the rest of the airfoil. At a sufficiently high incidence, the bubble bursts and leading-edge stall ensues. Results for a case in which both trailing-edge and leading-edge stall occur are shown in Figure 16, where the loading and the separation point location x_s are plotted against time for pitching up to 18 degrees. Note that very little C_n overshoot is predicted in this case.

As expected, a further increase in Reynolds number to 6×10^6 increases the resistance to both leading-edge and trailing-edge stall, although the effect appears to be somewhat exaggerated. When the steady-state pitch angle is 15.8 degrees, the separation point is only about .1c from the trailing edge. At a slightly larger pitch angle, that point moves rapidly up the chord. Figure 17 shows the loading and x_s variations with time for pitching up to 16.3 degrees. The steady-state separation point is seen to be about .35c from the leading edge in this case. No C_n overshoot at all is predicted for this case.

Leading-edge stall ultimately occurs at high pitch angles for $Re_c = 6 \times 10^6$, as well, but the separation point of the turbulent boundary layer very nearly encroaches on the leading-edge bubble before the bubble bursts. The distance separating them is only about .01c.

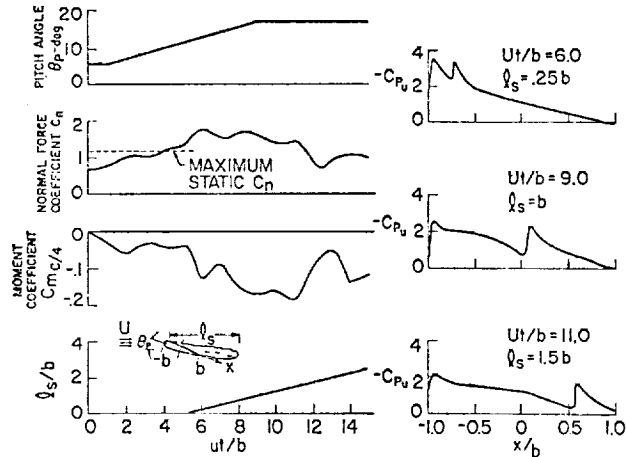


Figure 14. LOADING DURING TRANSIENT PITCHING
 $\theta_p b/U = .025$

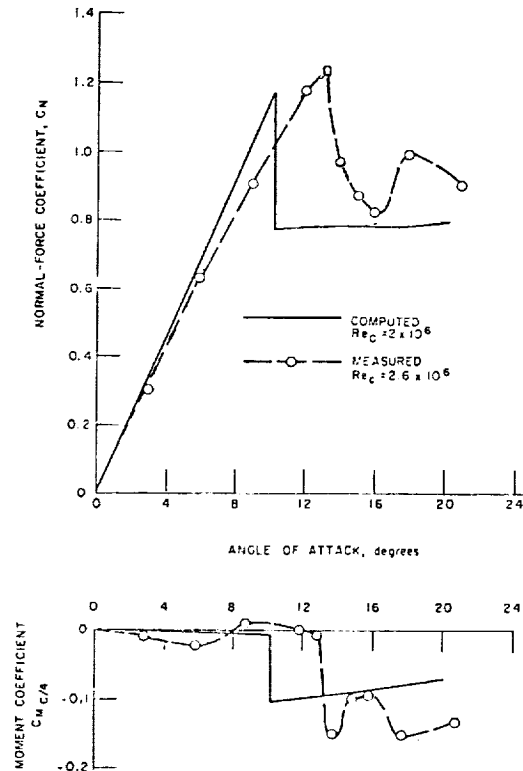


Figure 15. STATIC NORMAL FORCE AND MOMENT COEFFICIENTS (MEASURED RESULTS FROM REF. 8)

Results are summarized in Figure 18, which shows the computed variation of static normal-force and moment coefficients with angle of attack for the three Reynolds numbers considered. A flagged symbol indicates that the airfoil was undergoing trailing-edge stall. Results of measurements for different Reynolds numbers for the section analyzed are not available. However, data in Reference 41 show that a regular 0012 section at Reynolds numbers between 3 and 6 million has a maximum lift coefficient of about 1.6, generated at an angle of attack of 16 degrees, which agrees fairly well with the computed values of maximum C_n of 1.7 at $Re_c = 3 \times 10^6$ and 1.8 with $Re_c = 6 \times 10^6$, also occurring at about 16 degrees angle of attack.

The rapid falloff in normal force with angle of attack at higher Reynolds numbers is quite different from the behavior of thicker airfoils undergoing trailing-edge stall, the falloff in the latter case being more gradual (see Ref. 22). The reason for the sharp drop-off is apparently that the pressure rise is quite steep near the leading-edge but relatively flat aft of midchord. Thus, the separation point moves rapidly forward, once incipient separation occurs, until it encounters the region of steep gradients near midchord (note the variation of x_s in Figures 16 and 17). On thicker airfoils, the pressure increase along the chord is more uniform, allowing the separation point to stabilize at points closer to the trailing edge.

Sinusoidal Pitching Motions

The computed variations of normal-force and moment coefficient with pitch angle during sinusoidal pitching at a Reynolds number of two million are compared with measured results, from Reference 8, for reduced frequencies of 0, .13 and .26 in Figure 19. The predicted amounts of lift overshoot and their variation with reduced frequency are seen to agree quite well with the test results. The primary discrepancy is in the prediction of the loading when the airfoil is completely stalled and has a large negative pitch rate, which can be attributed to the assumption of quasi-steady flow in the analysis of the trapped-air region.

The predicted amounts of lift overshoot and their variation with reduced frequency are seen to agree quite well with the test results. The primary discrepancy is in the prediction of the loading when the airfoil is completely stalled and has a large negative pitch rate, which can be attributed to the assumption of quasi-steady flow in the analysis of the trapped-air region.

5. APPLICATIONS TO HELICOPTER AEROELASTIC PROBLEMS

Two different problems related to blade stall were analyzed, as described below. Consideration was limited to leading-edge stall with chordal Reynolds number equal to two million. Because the analyses were undertaken at a relatively early stage in the development of the theory, the free-stream speed was used as the rate of growth of the trapped-air region at stall onset. Consequently, the amounts of lift overshoot obtained were considerably less than would actually occur. It is believed that the results were not seriously affected, however, because the degree of freedom of primary concern during unsteady stall, blade torsional deflection, receives its excitation from the aerodynamic moment, which was reasonably well represented.

Analysis of Wake-Induced Stall

Large high-frequency oscillations in pressure, torsional moment, lift and aerodynamic moment on the retreating side were detected in flight-test data taken from a rotor blade during a maneuver, as shown in the plots of Figures 20 and 21 taken from Reference 42. It was asserted in Reference 42 that this response was the result of dynamic stall induced by previously formed tip vortices which, under the maneuver flight condition, pass under the blade at the azimuth positions indicated in Figures 20 and 21. To test this hypothesis, a series of calculations were carried out of blade loading resulting from passage over a series of three vortices of a two-dimensional airfoil with the section depicted in Figure 13. The airfoil was free to pitch about its quarter-chord, with spring restraint and inertia chosen to give a pitch natural frequency of 40 Hz. Computed pitch angle, lift and aerodynamic moment for vortex streamwise spacings of 8 chord lengths (giving a reduced encounter frequency of .39) and vertical spacing of one semi-chord are plotted in Figure 22.

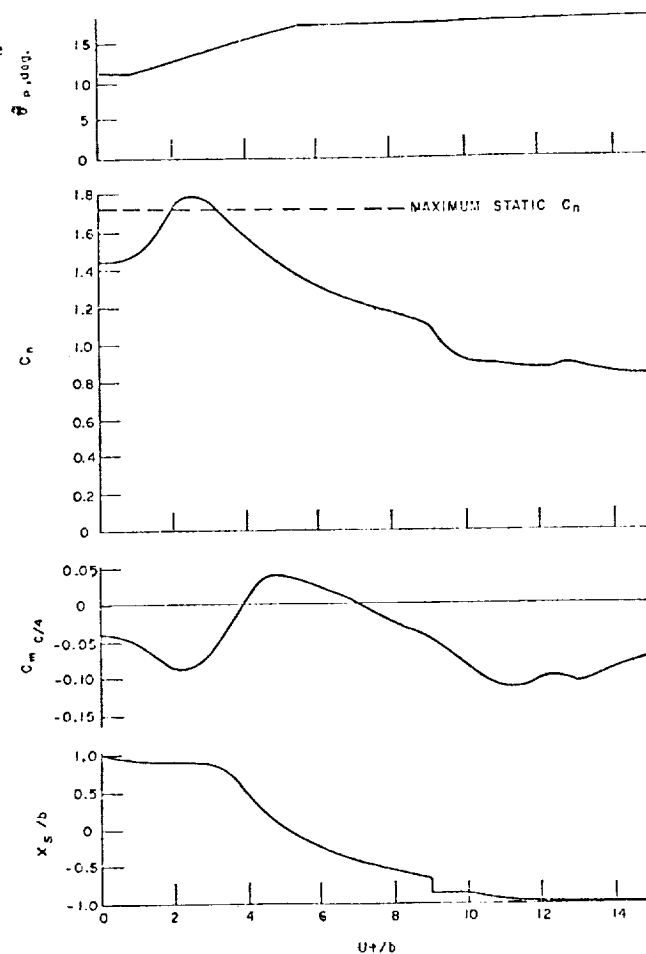


Figure 16. LOADING AND x_s VARIATION DURING TRANSIENT PITCH, $Re_c = 3 \times 10^6$, $\dot{\theta}_p b/U = .025$

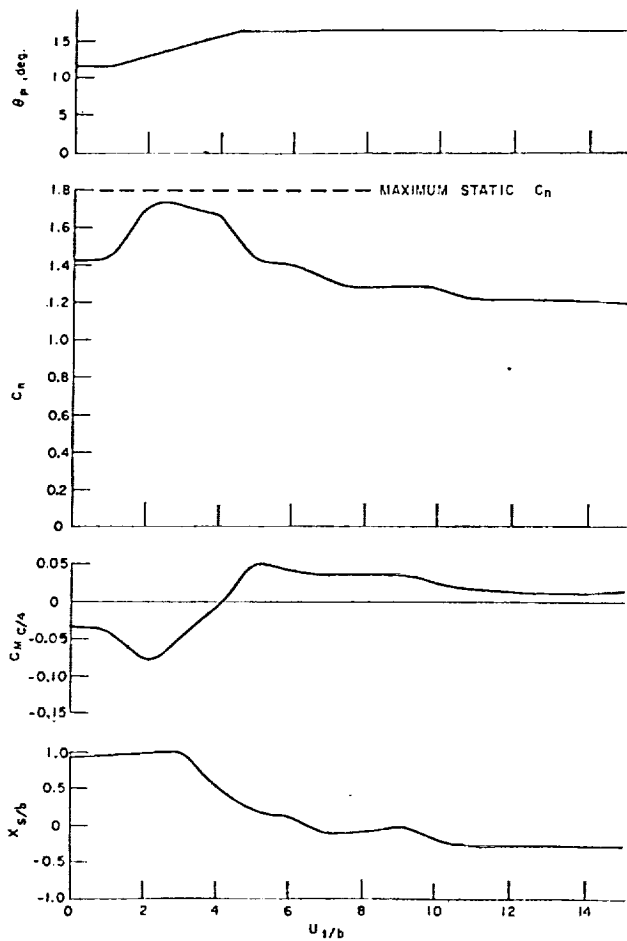


Figure 17. LOADING AND x_s VARIATION DURING TRANSIENT PITCH, $Re_c = 6 \times 10^6$

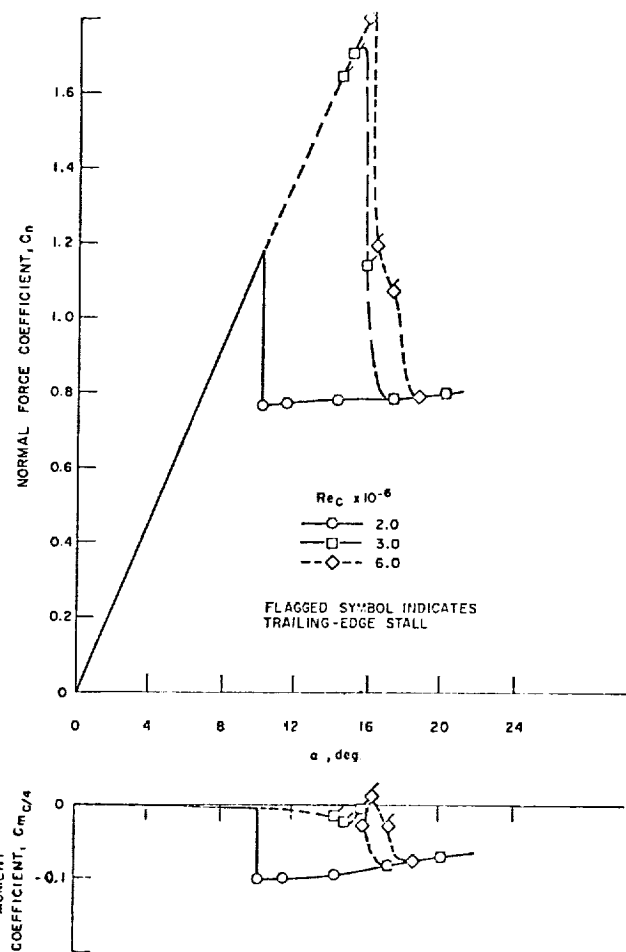


Figure 18. COMPUTED STATIC NORMAL-FORCE AND MOMENT COEFFICIENTS

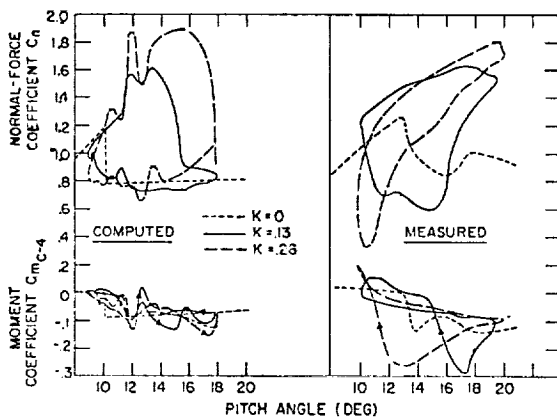


Figure 19. COMPARISON OF COMPUTED AND MEASURED LOADING DURING SINUSOIDAL PITCHING (MEASURED RESULTS FROM REF. 8)

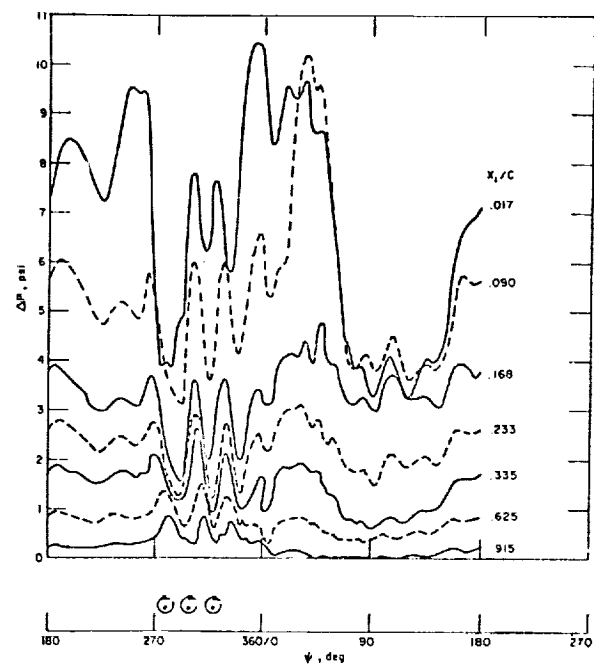


Figure 20. MEASURED DIFFERENTIAL PRESSURE TIME HISTORIES FOR THE 95% BLADE RADIUS IN A 1.5g PULLUP MANEUVER AT AN ADVANCE RATIO OF 0.22 (FROM REF. 42)

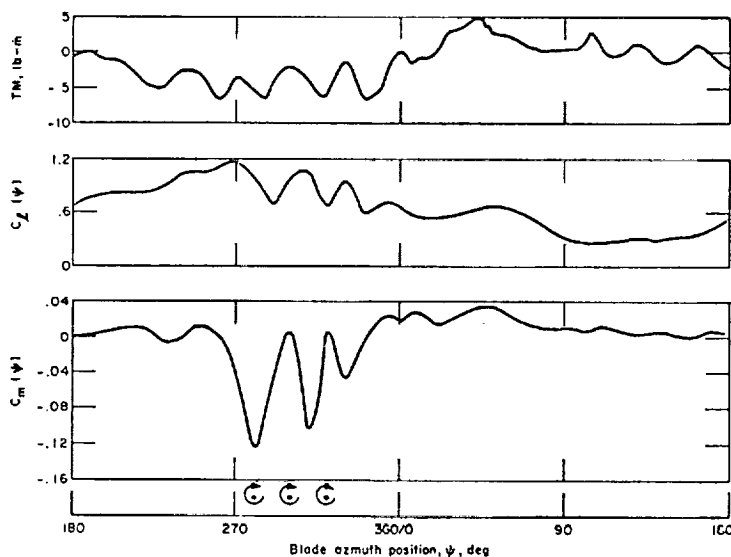


Figure 21. MEASURED TIME HISTORY OF SECTION LOADING AND MOMENT COEFFICIENT AND BLADE TORSIONAL RESPONSE FOR A 1.5g PULLUP (FROM REF. 42)

In comparing Figures 21 and 22, it should be noted that the large pitch oscillations in Figure 22 are about the pitch natural frequency (reduced frequency of .36) as are the torsional-moment oscillations in Figure 21 for azimuth angles between 270 and 360 degrees. Also, the computed high-frequency variation in lift and moment (at three to four times the pitch natural frequency) probably could not have been detected by the instrumentation employed in the flight-test measurements.

From the similarity of the curves, it would appear that the hypothesized mechanism is causing the large high-frequency response of the blade. This is further borne out by the computed differential pressures at selected chordwise stations shown plotted as a function of time in Figure 23, which exhibits the same phase shifts (time delays) in pressure drop with chordwise position as do the measured pressures (Figure 20). The results further explain why the oscillation is at the pitch natural frequency, rather than at the excitation frequency corresponding to the vortex spacing. The large nose-down moment exerted on the airfoil when it stalls causes the blade to rapidly pitch down and unstall. It was found in the computations that the blade only travels one or two semichords between stall onset and the beginning of flow reattachment. Thus, the blade is effectively excited by a series of discrete impulses, causing it to oscillate at its natural frequency.

Analysis of Stall Flutter

As was noted in Section 1, the occurrence of large-amplitude torsional oscillations and excessive control-linkage loads associated with blade stall have been of particular concern recently. The problem has prompted a number of studies of the effects of stall on blade dynamics (e.g., Refs. 1, 17 and 18). While stall has been identified as a causal element, the nonlinearity of the stall process, coupled with the unsteady aerodynamic environment, has precluded an analysis to the depth required to gain a thorough understanding of the mechanisms involved. In particular, it has not been clear whether the blade undergoes a true aeroelastic instability, a simple forced response, or some hybrid phenomenon which takes on the character of one or the other extreme, depending on flight conditions and blade vibrational characteristics. The study to be described was carried out in an attempt to shed some light on this aspect of the problem.

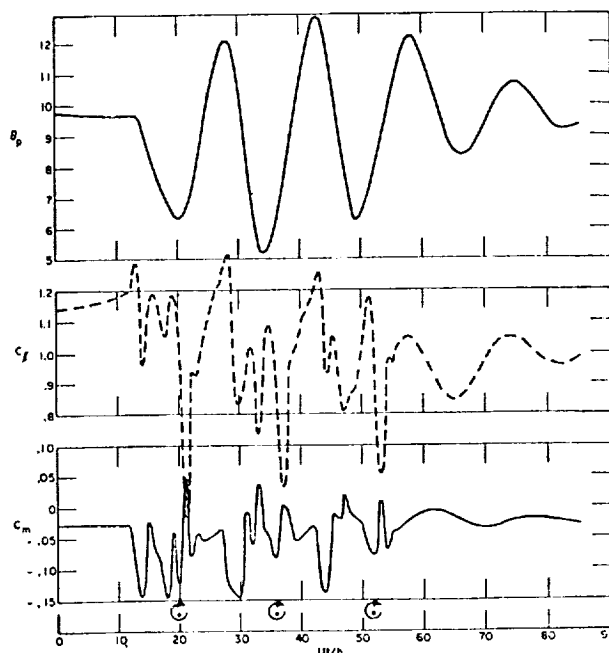


Figure 22. COMPUTED LOADING TIME HISTORY FOR VORTEX INDUCED STALL

Elastomechanical representation - Flapping, flapwise bending and torsional degrees of freedom were considered. The equations of motion of the rotor blade can be written in the form (see Ref. 43):

$$\sum_{j=1}^3 (M_{ij} \ddot{q}_j - \Omega^2 T_{ij} q_j) + K_i q_i = F_i \quad i=1, 2, 3$$

where q_1 is tip displacement due to flapping, q_2 is tip displacement due to first-mode bending and q_3 is angular tip displacement due to first-mode torsion. The uncoupled natural frequencies of those degrees of freedom are then given, respectively, by

$$\begin{aligned} \omega_\beta^2 &= -\Omega^2 T_{11}/M_{11} \quad (K_1 = 0), \\ \omega_\theta^2 &= \omega_{\theta_0}^2 - \Omega^2 T_{22}/M_{22} \quad (\omega_{\theta_0}^2 = K_2/M_{22}), \\ \omega_\phi^2 &= \omega_{\phi_0}^2 - \Omega^2 T_{33}/M_{33} \quad (\omega_{\phi_0}^2 = K_3/M_{33}) \end{aligned}$$

The generalized mass and centrifugal-force coefficients are integrals over the blade span involving the blade inertial properties and vibrational mode shapes (see, for example, Ref. 43).

The complexity of the aerodynamic representation precludes evaluation of the generalized forces by the usual strip approximation. It was felt essential, however, to retain both translational degrees of freedom in the investigation of the forward-flight problem, so a simple two-dimensional model of the dynamics could not be used. Therefore, a two-dimensional airfoil suspended in such a way as to have three degrees of freedom was analyzed. Inertial and stiffness parameters were assigned to make the coupled natural frequencies of the two-dimensional system match those of the rotor blade.

The system analyzed is shown schematically in Figure 24. The matching of the two-dimensional system with the blade dynamics proceeds as follows. Three generalized coordinates are first defined to correspond to those of the blade. Clearly, angular displacement θ_1 should correspond to blade torsional displacement at the blade tip. The counterparts of flapping and bending, Z_β and Z_θ , respectively, are defined by

$$Z_\beta = A_1 h_1 + B h_2, \quad Z_\theta = A_2 h_1 - B h_2$$

where

$$\begin{aligned} A_1 &= \frac{\omega_\beta^2 - \omega_2^2}{\omega_\theta^2 - \omega_\beta^2} & A_2 &= \frac{\omega_2^2 - \omega_\theta^2}{\omega_\theta^2 - \omega_\beta^2} \\ B &= \frac{(\omega_2^2 - \omega_\theta^2)(\omega_2^2 - \omega_\beta^2)}{(\omega_\theta^2 - \omega_\beta^2)\omega_2^2} \end{aligned} \quad (17)$$

and $\omega_i^2 = k_i/m_i$, $i = 1, 2$. With the above definitions, $\ddot{Z}_\beta + \omega_\beta^2 Z_\beta = -\ddot{h}_1$, to give the correct translational correspondence. It can further be shown that the uncoupled natural frequencies of the two-dimensional system match those of the blade, provided

$$(k_\theta + k_1 l_{s1}^2 + k_2 l_{s2}^2)/I_0 = \omega_\theta^2$$

while ω_1^2 and ω_2^2 satisfy

$$\begin{aligned} \omega_1^2 \omega_2^2 &= \omega_\theta^2 \omega_\beta^2, \\ \omega_1^2 + (1 + m_2/m_1) \omega_2^2 &= \omega_\theta^2 + \omega_\beta^2 \end{aligned} \quad (18)$$

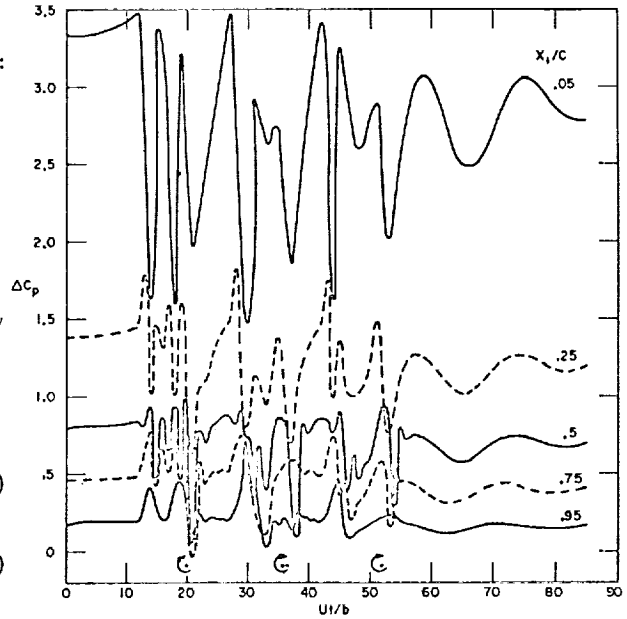


Figure 23. COMPUTED PRESSURE TIME HISTORIES FOR WAKE INDUCED STALL

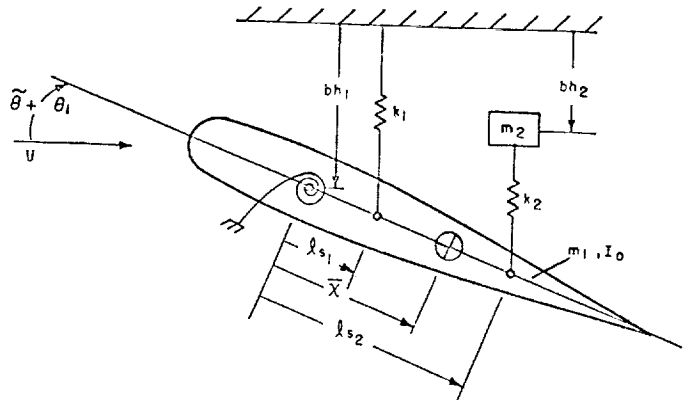


Figure 24. TWO-DIMENSIONAL ELASTOMECHANICAL SYSTEM

By comparing the generalized masses of the two systems, it follows that

$$m_1 b^2 / I_o = -A_1 M_{11} b^2 / (M_{33} R^2)$$

$$A_2 / A_1 = M_{11} / (M_{22} R^2) \equiv \lambda_m$$

The last relation, together with Eqs. (17) and (18) fixes m_2 / m_1 :

$$m_2 / m_1 = \frac{(1 + \lambda_m)(\omega_\phi^4 + \lambda_m \omega_\beta^4)}{(\lambda_m \omega_\beta^2 + \omega_\phi^2)^2} - 1$$

Equating the corresponding coefficients of the characteristic equations of the two systems provides three additional relations, which can be solved for the coupling parameters \bar{x} , l_{s1} , and l_{s2} . That calculation is outlined in Appendix B.

To complete the matching, quasi-steady approximations to the damping terms of the flapping equations are equated with the result that

$$m_1 R / (-A_1) = 4 \frac{r_R}{R} \frac{M_{11}}{R^2 [1 - (r_a/R)^4]}$$

$$U/U_o = 1 + \frac{4}{3} \left[\frac{1 - (r_a/R)^2}{1 - (r_a/R)^4} \right] \mu \sin \psi$$

where $\Omega r_R = U_o$. The aerodynamic reference radius r_R was selected to be .75R.

The angle of zero restraint in torsion was varied periodically to approximate the effects of cyclic pitch variation in forward flight, according to the formula

$$\tilde{\theta} = \theta_o [1 - 2 (R/r_R) \mu \sin \psi]$$

This variation gives nominally constant lift.

The equations of motion were solved by integrating analytically, using linear extrapolations to approximate the variation of lift and aerodynamic moment over the interval of integration. This scheme was found to give satisfactory results, provided the time interval of integration is no longer than about one fifth of the period of the coupled mode having the highest natural frequency.

Configuration analyzed - Vibrational and aerodynamic characteristics of the blade analyzed were selected to correspond to those of the model rotor blade described in Reference 43. That blade is untwisted, of constant chord, with $b/R = .0435$, $r_a/R = .174$, $\omega_\theta / \omega_\phi = 3.69$ and $x_m/b = .216$.

The test blade had a NACA 23012 section. The variation of static lift and moment coefficients with angle of attack for this section were computed from a series of transient pitch calculations and are shown in Figure 25, together with the measured section characteristics, from Reference 41. The aerodynamic model is seen to give nearly the correct maximum lift, but at a slightly lower angle of attack, and as indicated from the variation of $C_m c/4$, the computed center of pressure is somewhat further aft than that of the actual airfoil section below the stall angle.

Stability in hover - Initial calculations were performed for hovering flight, to allow a direct comparison with the test results of Reference 44 and to verify that the analytic models are capable of reproducing both classical and stall flutter. First, rotor speed was varied parametrically, with the collective pitch at a value well below the stall incidence. A classical bending-torsion instability was encountered at

$\Omega^* \approx \Omega R / (\omega_\theta b) = 5.3$ with $\omega_f / \omega_\theta = .803$. The variation of bending, flapping, and torsional displacements with azimuth angle at flutter onset are shown in Figure 26. By way of comparison, the tests yielded classical flutter at about $\Omega^* = 7.1$ with $\omega_f / \omega_\theta = .72$. These differences between analysis and test results can be attributed in large part to the use of a two-dimensional aerodynamic model, which cannot precisely reproduce the aerodynamic coupling between the rotational and translational degrees of freedom.

Susceptibility of the system to stall flutter was investigated next. It was found that a torsional limit cycle, at approximately the highest coupled natural frequency of the system, could be triggered for Ω^* as low as 3.4. Computed blade motions for stall flutter at Ω^* of 3.5 are shown in Figure 27.

For Ω^* below 3.4, a limit cycle could not be set up, regardless of the initial conditions or the collective pitch angle. Severe oscillations involving repeated stall and unstall could be made to occur by imposing a large initial bending deflection. However, the flapping response modulated the torsional

response, and caused continuous stall and/or unstall of the blade over a significant portion of a revolution, due to the large plunging rate generated by the flapping motion. An example of this occurrence is shown in Figure 28. Thus, while stall flutter involves only the rotational degree of freedom, the results obtained indicate that the minimum speed for its occurrence is determined by coupling with a translational degree of freedom.

Stability in forward flight - The blade was analyzed next for an advance ratio μ of .1. Computations were carried out in the same sequence as for hover. First, the rotational speed at which classical flutter occurs was determined. Then, stall-related instabilities were investigated.

A linear bending-torsion instability of the Floquet type (Ref. 45) was encountered at $\Omega^* = 5.2$. Blade motions as a function of azimuth angle at flutter onset are shown in Figure 29. The torsional and bending displacements are seen to display the aperiodic character typical of this type of instability. The flapping motion is the steady-state response to the cyclic pitch variation.

An instability analogous to stall flutter in hover was found to occur for Ω^* as low as about 4.4, with collective pitch angle greater than 12 degrees. Blade motions for $\Omega^* = 4.8$ are shown in Figure 30. The torsional displacement time history, while not strictly periodic, is nonetheless brought about by successive stall and unstall. The azimuth positions at which those events occur are marked by (S) and (U), respectively, on the ψ -scale.

The blade motions for the type of instability shown in Figure 30 are not of the same character as those of particular concern in the limiting of helicopter performance, in that the excessive torsional displacements shown in Figure 30 persist over a complete revolution of the blade. The control load time history taken from flight test (Ref. 18), shown in Figure 31 illustrates the type of stall-related blade motions usually encountered at a thrust level or forward speed near the upper limit of an aircraft.

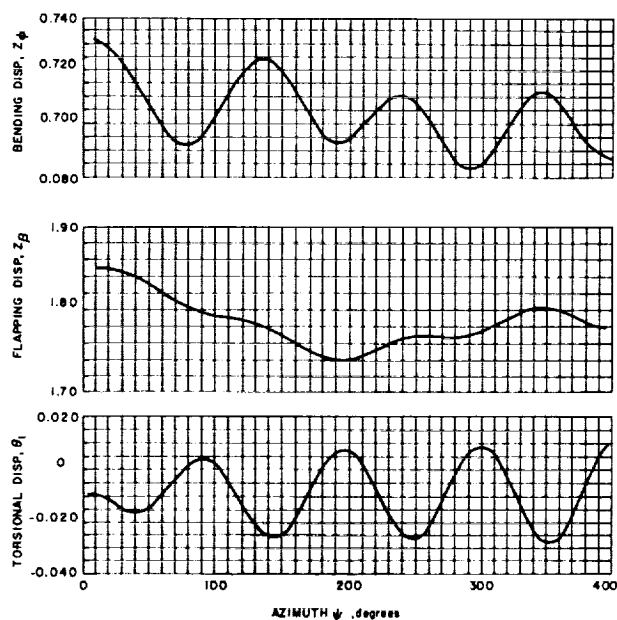


Figure 26. DISPLACEMENT TIME HISTORIES AT CLASSICAL FLUTTER ONSET - $\Omega^* = 5.3$, $\mu = 0$, $\theta_0 = 6^\circ$

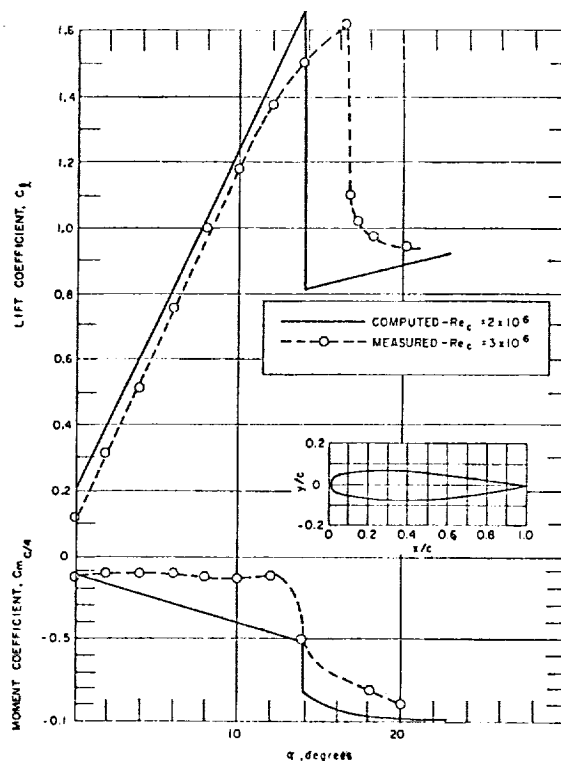


Figure 25. AIRFOIL SECTION CHARACTERISTICS FOR NACA 23012

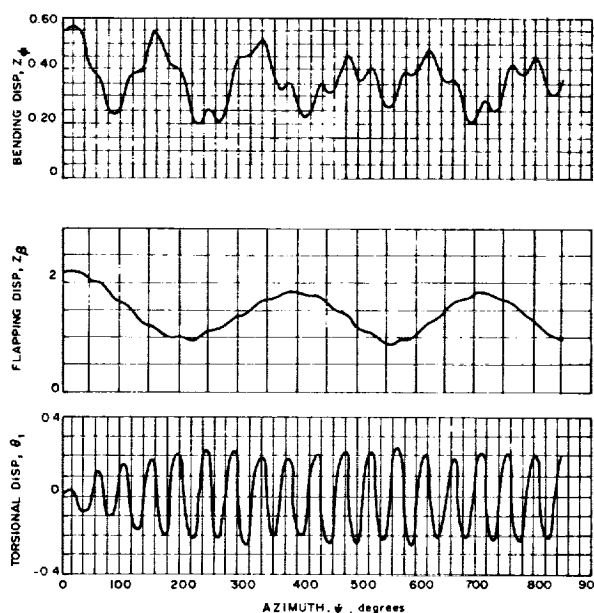


Figure 27. DISPLACEMENT TIME HISTORIES FOR STALL FLUTTER - $\Omega^* = 3.5$, $\theta_0 = 15^\circ$

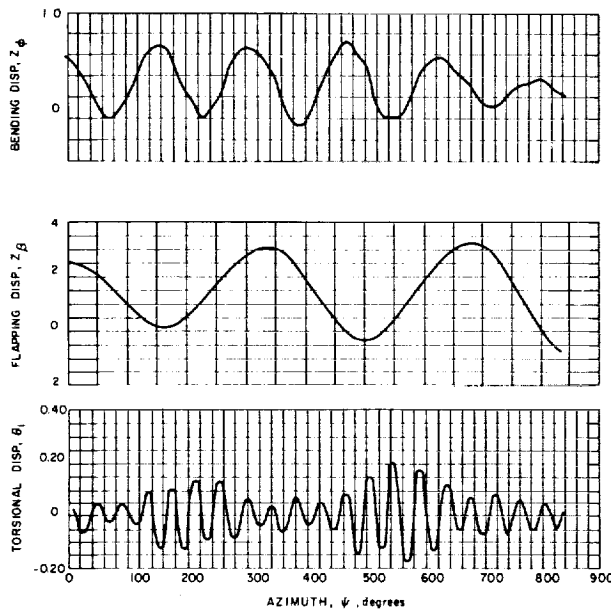


Figure 28. DISPLACEMENT TIME HISTORIES BELOW STALL FLUTTER BOUNDARY - $\Omega^* = 3.1$, $\theta_0 = 15$ DEGREES, $\mu = 0$

Large oscillations in the control loads, presumably deriving from blade torsional oscillations, are seen to persist only between about $\psi = 270$ degrees and $\psi = 400$ degrees, rather than throughout a complete revolution of the blade.

A torsional displacement time history more closely resembling the variation of control loads in Figure 31 was obtained for Ω^* less than 4.4, for collective pitch angles between 12 and 13 degrees. Results for a typical case are shown in Figure 32. The occurrences of stall and unstall are indicated on the abscissas. The large oscillations in torsion are clearly related to stall, but their persistence is not the result of successive stalling and unstalling as would be the case for true stall flutter. The blade appears to be responding to the sudden changes in aerodynamic moment at stall onset and unstall, as can be seen by comparing the variation of moment coefficient shown in Figure 32 with that of torsional displacement, and noting the azimuth positions at which stall and unstall occur. There is some cyclic stall-unstall within the stall zone evident in the results on the second and third revolutions. However, the major contributors to the oscillations appear to be the initial and final pulses associated with stall and unstall upon entering and leaving the zone. There are, in general, two cycles of torsional oscillation of excessive amplitude after the blade unstalls the last time on a given revolution. The severity of the response is apparently due in part to the suddenness of load changes at stall and partly to the relative lack of aerodynamic damping in pitch, particularly when the blade is not stalled.

It could be argued that the blade torsional oscillations of Figure 32 are still a manifestation of stall flutter, even though successive stall and unstall is not taking place, since the aerodynamic moment can undergo unstable variations when the blade remains stalled throughout a cycle (Ref. 8). It may, in fact, be the case that the large deflections do result partly from that effect, so choosing to term

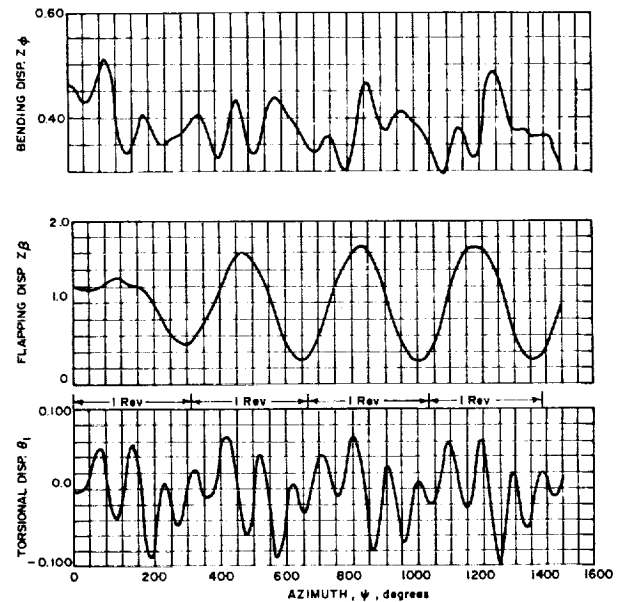


Figure 29. DISPLACEMENT TIME HISTORIES AT LINEAR INSTABILITY ONSET - $\Omega^* = 5.2$, $\theta_0 = 6$ DEGREES, $\mu = .1$

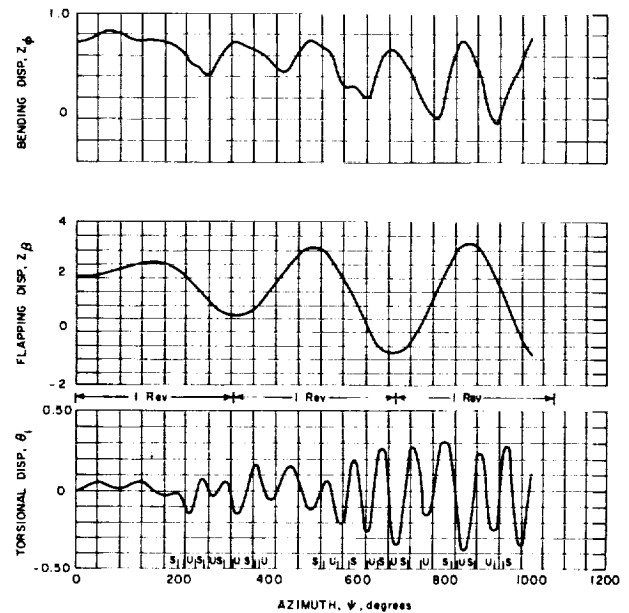


Figure 30. DISPLACEMENT TIME HISTORIES FOR STALL FLUTTER - $\Omega^* = 4.8$, $\theta_0 = 13$ DEGREES, $\mu = .1$

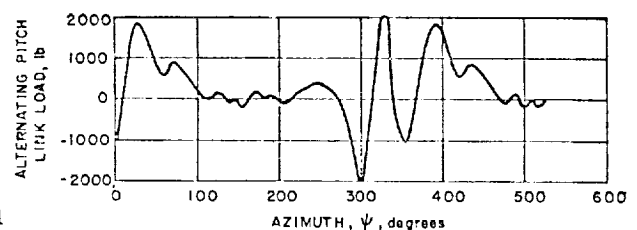


Figure 31. VARIATION IN PITCH LINK LOAD IN FLIGHT TEST OF CH47 AT 123 KNOTS (FROM REF. 18)

them as a simple response may be somewhat misleading. On the other hand, the solutions are distinctly different from what is definitely stall flutter obtained both in hover (Fig. 27) and in forward flight (Fig. 30) so that label would seem to be even less appropriate. Further, the persistence of the oscillations after exit from the stall zone is clearly symptomatic of a response, so, for lack of a more precise term, solutions of the type shown in Figure 32 are identified in what follows as excessive response.

Stall flutter and response boundaries - The effect of forward speed on stall-related instabilities was investigated by systematically varying the collective pitch angle and advance ratio, with Ω^* equal to 3.89. In order to relate the results to rotor performance, a mean lift coefficient \bar{C}_L is defined, according to

$$\bar{C}_L = \frac{\bar{l}}{\rho \Omega^2 R^2 b}$$

where \bar{l} is the time-averaged lift per unit span at the aerodynamic reference radius. This coefficient is, to a good approximation, directly proportional to the thrust coefficient (see Ref. 46).

The results obtained are summarized in Figure 33 as a plot of \bar{C}_L vs μ . As thrust is increased at a given μ , the rotor is seen to first encounter a region of excessive response, of the type discussed previously, and then, for μ of .2 or less, a region where stall flutter occurs. Increasing advance ratio has the effect of suppressing the tendency for stall flutter. At $\mu = .2$, stall flutter occurs at $\bar{C}_L = .85$, but a further increase in \bar{C}_L results in excessive response again. At $\mu = .3$ a limit-cycle type of oscillation could not be triggered at all. As a result, stall flutter is confined to a region somewhat as indicated by the shaded area in Figure 33.

The suppression of stall flutter at high advance ratio is apparently caused by an effect similar to the one encountered at low rotor speed in hover, whereby the flapping motion prevented a limit cycle from occurring. This can be seen from the blade motions obtained for $\mu = .3$ and $\bar{C}_L = .78$, plotted in Figure 34. On the first revolution, as the blade enters the stall zone on the retreating side, it appears that a limit cycle is being set up, with repeated stall and unstall occurring. However, at about $\psi = 420$ degrees, the flapping motion has built up in response to the large cyclic pitch changes, producing a negative plunging rate sufficient to keep the blade unstalled over the remainder of its passage on the advancing side. Then, when the blade again enters the stall zone, the large positive flap-induced plunging rate precludes unstall until exit from the stall zone at about $\psi = 670$ degrees. As a result, the blade subsequently undergoes excessive torsional response, rather than stall flutter.

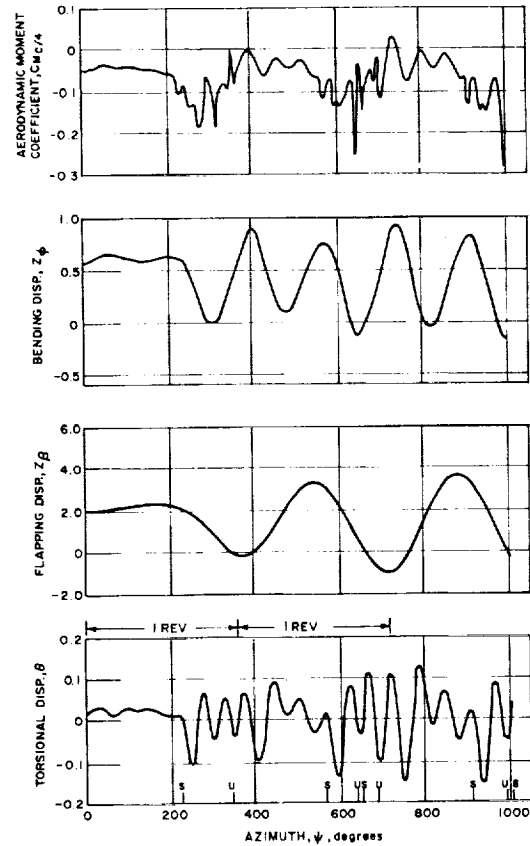


Figure 32. DISPLACEMENT AND MOMENT TIME HISTORIES FOR EXCESSIVE TORSIONAL RESPONSE
 $\Omega^* = 3.89$, $\theta_0 = 12$ DEGREES, $\mu = .1$

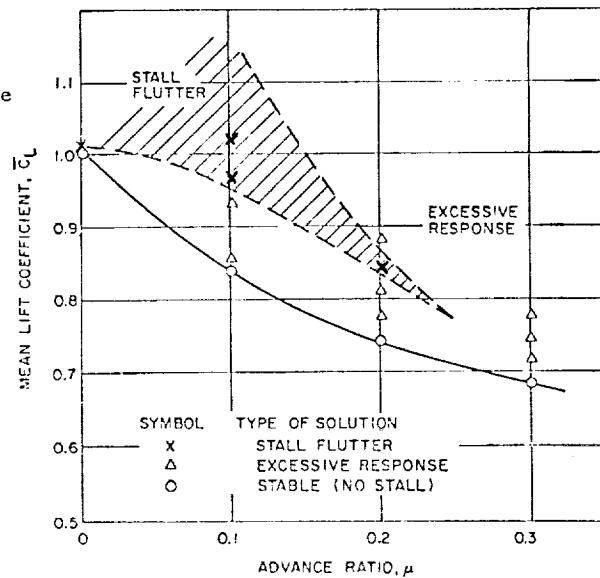


Figure 33. STALL STABILITY BOUNDARIES FOR
 $\Omega^* = 3.89$

6. RECOMMENDATIONS FOR FURTHER RESEARCH

The need for further study is indicated in the following areas.

Unsteady Viscous Effects

From the comparison of computed and measured loading during sinusoidal pitching, it was concluded that once an airfoil is completely stalled, the pressure in the trapped-air region is strongly influenced by unsteady effects. As a further indication that this must be the case, data in Reference 8 show that an oscillating airfoil which is completely stalled throughout the cycle undergoes a large lift hysteresis. Both theoretical and experimental studies are needed to determine the major contributors to this effect.

Leading-Edge Bubble

Despite much conjecture and considerable study, the actual mechanism for bubble bursting remains undefined. A major step in resolving the problem would be to determine what factors are controlling where transition occurs in the laminar shear layer. An interesting adjunct to the research would be a study of the influence of suction or other similar techniques on bubble bursting, which would be applicable to possible active prevention or delay of leading-edge stall.

Stall Onset and Unstall Processes

Experiments are needed to define the details of the processes of formation and wash-off of the trapped-air region during unsteady leading-edge stall so that workable analytic models can be formulated.

7. REFERENCES

1. Ham, N. D. and Young, M. I., "Torsional Oscillation of Helicopter Blades Due to Stall," J. Aircraft, Vol. 3, No. 3, May-June 1966, pp. 218-224.
2. Reding, J., and Ericsson, L., "Review of Delta Wing Space Shuttle Vehicle Dynamics," Lockheed Missiles and Space Co. Rept. No. D243938, October 1971.
3. Emmons, H. W., Kronauer, R. E. and Rockett, J. A., "A Survey of Stall Propagation - Experiment and Theory," J. of the ASME, J. of Basic Eng. (Series D), Vol. 31, Sept. 1959, pp. 409-416.
4. Schnittger, J. R., "Single Degree of Freedom Flutter of Compressor Blades in Separated Flow," J. Aero. Sci., Vol. 21, No. 1, January 1959, pp. 27-36.
5. Halfman, R., Johnson, H. and Haley, S., "Evaluation of High-Angle-of-Attack Aerodynamic-Derivative Data and Stall-Flutter Prediction Techniques," NACA TN 2533, November 1951.
6. Sisto, F., "Stall-Flutter in Cascades," J. Aero. Sci., Vol. 20, No. 9, September 1953, pp. 598-604.
7. Rainey, A. G., "Measurement of Aerodynamic Forces for Various Mean Angles of Attack on an Airfoil Oscillating in Pitch and on Two Finite-Spin Wings Oscillating in Bending with Emphasis on Damping in the Stall," NACA TR 1305, 1957.
8. Liiva, J., Davenport, F., Gray, L. and Walton, I., "Two-Dimensional Tests of Airfoils Oscillating Near Stall - Vol. 1, Summary and Evaluation of Results," USAAVLABB Tech. Rept. 68-13A, April 1968.
9. Velkoff, H., Blaser, D. and Jones, K., "Boundary-Layer Discontinuity on a Helicopter Rotor Blade in Hovering," J. Aircraft, Vol. 8, No. 2, February 1971, pp. 101-107.
10. Dwyer, H. A. and McCroskey, W. J., "Crossflow and Unsteady Boundary-Layer Effects on Rotating Blades," AIAA J., Vol. 9, No. 8, August 1971, pp. 1498-1505.

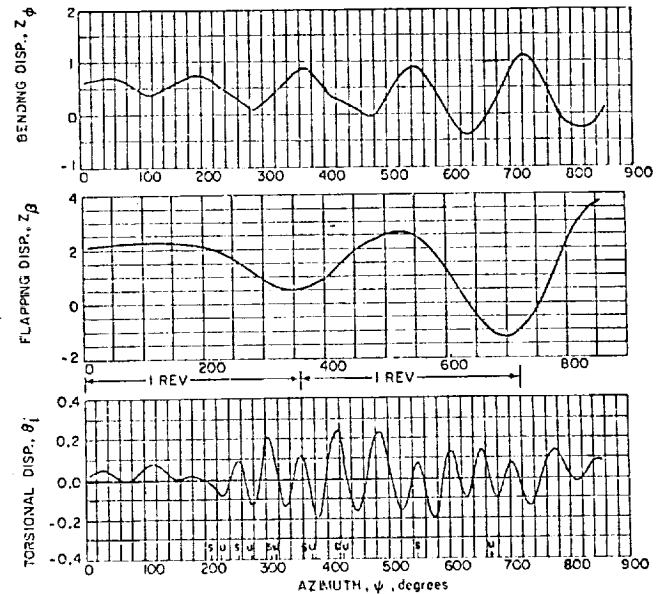


Figure 34. DISPLACEMENT TIME HISTORIES AT HIGH ADVANCE RATIO - $\Omega^* = 3.89$, $\bar{C}_L = .78$, $\mu = .3$

11. McCroskey, W. J. and Fisher, R. K., "Detailed Aerodynamic Measurements on a Model Rotor in the Blade Stall Regime," J. Am. Helicopter Soc., Vol. 17, No. 1, January 1972, pp. 20-30.
12. Martin, J. M., Empey, R. W., McCroskey, W. J., and Caradonna, F. X., Am. Helicopter Soc. Preprint No. 702, May 1973.
13. Patay, S. A., "Leading Edge Separation on an Airfoil During Dynamic Stall," M.I.T. ASRL TR 156-1, October 1969.
14. Woods, L. C., "Aerodynamic Forces on an Oscillating Airfoil Fitted with a Spoiler," Proc. Roy. Soc., Series A, Vol. 239, 1957, pp. 328-337.
15. Ham, N. D., "Aerodynamic Loading on a Two-Dimensional Airfoil During Dynamic Stall," AIAA J., Vol. 6, No. 10, October 1968, pp. 1927-1934.
16. Ericsson, L., and Reding, J., "Unsteady Airfoil Stall," NASA CR-66787, July 1969.
17. Carta, F. and Neibanck, C., "Prediction of Rotor Instability at High Forward Speeds - Vol. III, Stall Flutter," USAAVLABS TR 68-18C, February 1969.
18. Tarzanin, F. J., "Prediction of Control Loads Due to Blade Stall," J. Am. Helicopter Soc., Vol. 17, No. 2, April 1972.
19. Crimi, P. and Reeves, B. L., "A Method for Analyzing Dynamic Stall of Helicopter Rotor Blades," NASA CR-2009, May 1972.
20. Crimi, P., "Analysis of Stall Flutter of a Helicopter Rotor Blade," AIAA Paper No. 73-403, March 1973 (also, NASA CR, to be published).
21. Crimi, P., "Investigation of Nonlinear Inviscid and Viscous Flow Effects in the Analysis of Dynamic Stall," NASA CR, to be published.
22. McCullough, G. B., and Gault, D. E., "Examples of Three Representative Types of Airfoil-Section Stall at Low Speed," NACA TN 2502, September 1951.
23. Ward, J. W., "The Behavior and Effects of Laminar Separation Bubbles on Airfoils in Incompressible Flow," J. Roy. Aero. Soc., Vol. 67, December 1963, pp. 783-790.
24. Tani, I., "Low Speed Flows Involving Bubble Separations," Prog. in Aero. Sci., Vol. 5, Pergamon Press, 1964, pp. 70-103.
25. Rott, N., "Unsteady Viscous Flow in the Vicinity of a Stagnation Point," Quart. Appl. Math., Vol. 13, 1956, pp. 444-451.
26. Sears, W. R. and Telionis, D. P., "Unsteady Boundary-Layer Separation," Preprint, IUTAM Symposium on Unsteady Boundary Layers, Quebec, May 1971.
27. Lindsey, W. and Landrum, E., "Compilation of Information on the Transonic Attachment of Flows at the Leading Edges of Airfoils," NACA TN 4202, February 1958.
28. Peake, D. J., Rainbird, W. J. and Atraghji, E. G., "Three-Dimensional Flow Separations on Aircraft and Missiles," AIAA J., Vol. 10, No. 5, May 1972, pp. 567-580.
29. Chambers, J. R. and Bowman, J. S., "Recent Experience with Techniques for Prediction of Spin Characteristics of Fighter Aircraft," J. Aircraft, Vol. 8, No. 7, July 1971, pp. 549-553.
30. Lighthill, M. J., "A New Approach to Thin Airfoil Theory," Aeron. Quart., Vol. 3, November 1951, pp. 193-210.
31. Smith, A. M. O. and Cebeci, T., "Numerical Solution of the Turbulent-Boundary-Layer Equations," McDonnell-Douglas Rept. No. DAC33735, May 1967.
32. Schlichting, H., Boundary Layer Theory, Fourth Edition, McGraw-Hill, New York, 1960.
33. Meller, G. L. and Gibson, D. M., "Equilibrium Turbulent Boundary Layers," J. Fluid Mech., Vol. 24, No. 2, 1966, pp. 225-253.
34. van Driest, E. R. and Blumer, C. B., "Boundary Layer Transition: Free-Stream Turbulence and Pressure Gradient Effects," AIAA J., Vol. 1, No. 6, June 1963, pp. 1303-1306.

35. Todisco, A. and Reeves, B. L., "Turbulent Boundary Layer Separation and Reattachment at Supersonic and Hypersonic Speeds," Proc. Conference on Viscous Interaction Phenomena in Supersonic and Hypersonic Flow, USAF ARL, Wright-Patterson Air Force Base, Ohio, May 1969.
36. Hunter, L. G. and Reeves, B. L., "Results of a Strong-Interaction, Wake-Like Model of Supersonic Separated and Reattaching Turbulent Flows," AIAA Paper No. 71-128, January 1971.
37. Reeves, B. L. and Lees, L., "Theory of Laminar Near Wake of Blunt Bodies in Hypersonic Flow," AIAA J., Vol. 3, No. 11, November 1965, pp. 2061-2074.
38. Gault, D. E., "An Experimental Investigation of Separated Laminar Flow," NACA TN 3505, September 1955.
39. Horton, H. P., "A Semi-Empirical Theory for the Growth and Bursting of Laminar Separation Bubbles," ARC C.P. No. 1973, June 1967.
40. Carta, F. O., "A Theoretical Study of the Effect of Unsteady Pressure Gradient Reduction on Dynamic Stall Delay," J. Aircraft, Vol. 8, No. 10, October 1971, pp. 839-841.
41. Abbott, I. H. and Doenhoff, A. E., Theory of Wing Sections, Dover, New York, 1959.
42. Ward, J. F., "Helicopter Rotor Differential Pressures and Structural Response Measured in Transient and Steady-State Maneuvers," J. Am. Helicopter Soc., Vol. 16, No. 1, January 1971, pp. 16-25.
43. Gates, C., Piziali, R. and DuWaldt, F., "Comparison of Theoretical and Experimental Flutter Characteristics for a Model Rotor in Translational Flight," J. Am. Helicopter Soc., Vol. 8, No. 2, April 1963, pp. 14-27.
44. Brooks, G. W. and Baker, J. E., "An Experimental Investigation of the Effects of Various Parameters Including Tip Mach Number on the Flutter of Some Model Helicopter Rotor Blades," NACA TN 4005, September 1958.
45. Crimi, P., "Stability of Dynamic Systems with Periodically Varying Parameters," AIAA J., Vol. 8, No. 10, October 1970, pp. 1760-1764.
46. Gessow, A. and Meyers, G., The Aerodynamics of the Helicopter, Ungar, New York, 1967.
47. Muskhelishvili, N. I., Singular Integral Equations, P. Noordhoff, Groningen, 1953.

ACKNOWLEDGEMENTS

The analyses of the trapped-air region and the leading-edge bubble outlined in Section 3 were carried out by Dr. Barry L. Reeves of Avco Systems Division. The results presented here were obtained in large part under sponsorship of the NASA Langley Research Center and the U. S. Army Air Mobility Research and Development Laboratory - Langley Directorate.

APPENDIX A

SOLUTION FOR STALLED FLAT PLATE IN STEADY FLOW

First, consider the case with $x_R > b$. Equations (2) through (5) become, for steady flow with constant pressure p_d in the dead-air region:

$$\frac{1}{\pi} \int_{-b}^b \frac{\gamma(\xi) d\xi}{x - \xi} = 2 U a, \quad -b \leq x \leq x_s \quad (A-1)$$

$$\sigma(x) + \frac{1}{\pi} \int_{-b}^b \frac{\gamma(\xi) d\xi}{x - \xi} = 2 U a, \quad x_s \leq x \leq b \quad (A-2)$$

$$\gamma(x) + \frac{1}{\pi} \int_{x_s}^{x_R} \frac{\sigma(\xi) d\xi}{x - \xi} = \frac{2(p_\infty - p_d)}{\rho U} \quad x_s \leq x \leq b \quad (A-3)$$

$$\frac{1}{\pi} \int_{x_s}^{x_R} \frac{\sigma(\xi) d\xi}{x - \xi} = \frac{2(p_\infty - p_d)}{\rho U} \quad b \leq x \leq x_R \quad (A-4)$$

The first step is to reduce the number of equations by solving for γ on the interval $(-b, x_s)$ in Eq. (A-1) and solving for σ on the interval (b, x_R) from Eq. (A-4). Formally inverting these two singular integral equations (see Ref. 47), it is found that

$$\begin{aligned} \gamma(x) &= \frac{1}{\pi \sqrt{(x_s - x)(x + b)}} \left\{ \int_{-b}^{x_s} \frac{\left[2 U a - \frac{1}{\pi} \int_{x_s}^b \frac{\gamma(\lambda) d\lambda}{\xi - \lambda} \right] \sqrt{(x_s - \xi)(\xi + b)}}{\xi - x} d\xi + A \right\} \\ &= \frac{1}{\pi \sqrt{(x_s - x)(x + b)}} \left\{ A - 2 \pi U a x - \int_{x_s}^b \frac{\sqrt{(\lambda + b)(\lambda - x_s)}}{\lambda - x} \gamma(\lambda) d\lambda \right\} \end{aligned} \quad (A-5)$$

$$\begin{aligned} \sigma(x) &= \frac{1}{\pi \sqrt{(x_R - x)(x - b)}} \left\{ \int_b^{x_R} \left[\frac{2(p_\infty - p_d)}{\rho U} - \frac{1}{\pi} \int_{x_s}^b \frac{\sigma(\lambda) d\lambda}{\xi - \lambda} \right] \frac{\sqrt{(x_R - \xi)(\xi - b)}}{\xi - x} d\xi + B \right\} \\ &= \frac{1}{\pi \sqrt{(x_R - x)(x - b)}} \left\{ B' - \frac{2 \pi (p_\infty - p_d) x}{\rho U} - \int_{x_s}^b \frac{\sqrt{(x_R - \lambda)(b - \lambda)} \sigma(\lambda) d\lambda}{x - \lambda} \right\} \end{aligned} \quad (A-6)$$

where A' and B' are as yet undetermined constants. If Eqs. (A-5) and (A-6) are substituted in Eqs. (A-2) and (A-3), respectively, and certain of the resulting integrals are evaluated, the following pair of integral equations is obtained:

$$\sigma(x) + \frac{1}{\pi} \int_{x_s}^b \left[\frac{(z+b)(z-x_s)}{(x+b)(x-x_s)} \right]^{1/2} \frac{\gamma(z) dz}{x-z} = \frac{2 U a x - A'/\pi}{\sqrt{(x-x_s)(x+b)}} \quad (A-7)$$

$$\gamma(x) + \frac{1}{\pi} \int_{x_s}^b \left[\frac{(b-z)(x_R-z)}{(b-x)(x_R-x)} \right]^{1/2} \frac{\sigma(z) dz}{x-z} = \frac{B'/\pi - \left(\frac{2(p_\infty - p_d)}{\rho U} \right) x}{\sqrt{(x_R-x)(b-x)}} \quad (A-8)$$

It is required that σ be well behaved at $x = x_s$, which, from Eq. (A-7), allows the value of A' to be assigned:

$$\frac{A'}{\pi} = 2 U a x_s + \frac{1}{\pi} \int_{x_s}^b \sqrt{\frac{\eta+b}{\eta-x_s}} \gamma(\eta) d\eta$$

Equations (A-7) and (A-8) can be combined by formally solving Eq. (A-8) for σ :

$$\begin{aligned} \sqrt{(b-x)(x_R-x)} \sigma(x) &= \frac{1}{\pi \sqrt{(b-x)(x-x_s)}} \left\{ \int_{x_s}^b \left[\frac{B'}{\pi} - \frac{2(p_\infty - p_d)}{\rho U} z \right. \right. \\ &\quad \left. \left. - \gamma(z) \sqrt{(x_R-z)(b-z)} \right] \frac{\sqrt{(b-z)(z-x_s)}}{z-x} dz + C \right\} \\ &= \frac{1}{\pi \sqrt{(b-x)(x-x_s)}} \left\{ C - \int_{x_s}^b \gamma(z)(b-z) \frac{\sqrt{(z-x_s)(x_R-z)}}{z-x} dz \right. \\ &\quad \left. + \pi \left[\frac{B'}{\pi} - \frac{2(p_\infty - p_d)}{\rho U} x \right] \left[\left(\frac{b+x_s}{2} \right) - x \right] - \frac{2\pi(p_\infty - p_d)}{\rho U} \frac{(b-x_s)^2}{8} \right\} \end{aligned}$$

If σ is to be at least integrable at $x = b$, the quantity in brackets must vanish as $x \rightarrow b$. This provides a relation between the undetermined constants C and B' . The continuity of σ at $x = x_s$ provides the other relation needed to solve for those constants, with the result that

$$\sigma(x) = \sqrt{\frac{x-x_s}{x_R-x}} \left\{ \frac{1}{\pi} \int_{x_s}^b \frac{\gamma(z)}{(x-z)} \sqrt{\frac{x_R-z}{z-x_s}} dz - \frac{2(p_\infty - p_d)}{\rho U} \right\} \quad (A-9)$$

Substituting Eq. (A-9) and the relation for A' in Eq. (A-7), it is found that

$$\frac{1}{\pi} \int_{x_s}^b \frac{\gamma(z)}{x-z} \sqrt{\frac{x_R-z}{z-x_s}} \left\{ \sqrt{\frac{x+b}{x_R-x}} \sqrt{\frac{z+b}{x_R-z}} \right\} dz = 2 U a + \frac{2(p_\infty - p_d)}{\rho U} \sqrt{\frac{x+b}{x_R-x}} \quad (A-10)$$

Now, let

$$g(x) = (x_R - x) \sqrt{\frac{x+b}{x-x_s}} \quad \gamma(x)$$

$$z(x) = \sqrt{\frac{x+b}{x_R-x}}$$

With some manipulation of the integrand of Eq. (A-10), that relation can be written in the form

$$\frac{1}{\pi} \int_{x_s}^b \frac{g(\xi) [dz(\xi)/d\xi]}{z(x) - z(\xi)} d\xi = \frac{x_R + b}{1 + z^2(x)} \left[U_a + \frac{1}{\pi} \frac{(p_\infty - p_d)}{\rho U} z(x) \right] \quad (A-11)$$

This equation can be solved for g . Letting $z_s = z(x_s)$ and $z_b = z(b)$,

$$g(z) = \frac{1}{\pi} \sqrt{\frac{z_b - z}{z - z_s}} \int_{z_s}^{z_b} \sqrt{\frac{\xi - z_s}{z_b - \xi}} \left(\frac{x_R + b}{\xi^2 + 1} \right) [k_a + k_p \xi] \frac{d\xi}{\xi - z} \quad (A-12)$$

where the undetermined constant was assigned to make g well behaved at z_b and $k_a = U_a$, $k_p = (p_\infty - p_d)/\rho U$. If the integrand of Eq. (A-12) is expanded in partial fractions, the resulting integrals can be evaluated by standard methods. By substituting the result in previous relations, expressions for γ and σ over the whole interval for which they are defined can be obtained. The complete solution for $x_R > b$ is:

$$\gamma(x) = \frac{1}{z} \sqrt{\frac{z_s^2 - z^2}{1 + z_s^2}} \left[(C_0 + C_1 z) \sqrt{\frac{z_b - z}{z_s - z}} + (C_0 - C_1 z) \sqrt{\frac{z_b + z}{z_s + z}} \right], \quad -b \leq x \leq x_s;$$

$$\gamma(x) = \frac{1}{z} \sqrt{\frac{(z_b - z)(z + z_s)}{1 + z_s^2}} (C_0 + C_1 z), \quad x_s \leq x \leq b;$$

$$\sigma(x) = \frac{1}{z} (C_0 - C_1 z) \sqrt{\frac{(z - z_s)(z - z_b)}{1 + z_s^2}}, \quad x_s \leq x \leq b;$$

$$\sigma(x) = \frac{1}{z} \sqrt{\frac{z^2 - z_s^2}{1 + z_s^2}} \left[(C_0 - C_1 z) \sqrt{\frac{z + z_b}{z + z_s}} - (C_0 + C_1 z) \sqrt{\frac{z - z_b}{z - z_s}} \right], \quad b \leq x \leq x_R.$$

where

$$\begin{aligned} C_0 &= (k_a - k_p z_s) \mathcal{L}_0 + (k_p + k_a z_s) \mathcal{L}_1 \\ C_1 &= (k_a z_s + k_p) \mathcal{L}_0 - (k_a - k_p z_s) \mathcal{L}_1 \\ \mathcal{L}_n &= \left\{ \frac{\sqrt{(1 - z_s z_b)^2 + (z_s + z_b)^2 + (-1)^n (1 - z_s z_b)}}{2(1 + z_s^2)(1 + z_b^2)} \right\}^{1/2} \quad n = 0, 1. \end{aligned}$$

The solution for $x_R < b$ is obtained by an analogous procedure, there again being four coupled singular integral equations in σ and γ . An equation for γ on the interval (x_s, x_R) is obtained which is of exactly the same form as Eq. (A-12). Omitting the details, the solution for $x_R < b$ is:

$$\gamma(x) = \left[\frac{r_R^2 + 1}{r_s^2 + 1} \right] \left(\frac{r_s^2 - r^2}{r_R^2 - r^2} \right)^{1/2} \left\{ \left(\frac{\hat{C}_0}{r} + \hat{C}_1 \right) \sqrt{\frac{r_R - r}{r_s - r}} + \left(\frac{\hat{C}_0}{r} - \hat{C}_1 \right) \sqrt{\frac{r_R + r}{r_s + r}} \right\}, \quad -b \leq x \leq x_s;$$

$$\gamma(x) = \left[\left(\frac{r_R^2 + 1}{r_s^2 + 1} \right) \left(\frac{r + r_s}{r + r_R} \right) \right]^{1/2} \left(\frac{\hat{C}_0}{r} + \hat{C}_1 \right), \quad x_s \leq x \leq x_R;$$

$$\gamma(x) = \left[\left(\frac{r_R^2 + 1}{r_s^2 + 1} \right) \left(\frac{r^2 - r_s^2}{r^2 - r_R^2} \right) \right]^{1/2} \left\{ \left(\frac{\hat{C}_0}{r} + \hat{C}_1 \right) \sqrt{\frac{r - r_R}{r - r_s}} + \left(\frac{\hat{C}_0}{r} - \hat{C}_1 \right) \sqrt{\frac{r + r_R}{r + r_s}} \right\}$$

$$x_R \leq x \leq b;$$

$$\sigma(x) = \left[\left(\frac{r_R^2 + 1}{r_s^2 + 1} \right) \left(\frac{r - r_s}{r_R - r} \right) \right]^{1/2} \left(\frac{\hat{C}_0}{r} - \hat{C}_1 \right), \quad x_s \leq x \leq x_R$$

where

$$r(x) = \sqrt{\frac{b+x}{b-x}}$$

$$r_R = r(x_R)$$

$$r_s = r(x_s)$$

while \hat{C}_0 and \hat{C}_1 have the same definitions as C_0 and C_1 , respectively, but with z_s replaced by r_s and z_b replaced by r_R .

APPENDIX B

DETERMINATION OF COUPLING PARAMETERS

The characteristic equation for the rotor blade is

$$\sum_{k=0}^3 B_{2k} \lambda^{2k} = 0$$

where

$$\begin{aligned} B_0 &= f_0 - \frac{\bar{\omega}_\emptyset^2 T_{13}^2}{M_{11} M_{33}} - \frac{\bar{\omega}_\beta^2 T_{23}^2}{M_{22} M_{33}} \\ B_2 &= f_2 + 2 \frac{\bar{\omega}_\emptyset^2 M_{13} T_{13}}{M_{11} M_{33}} + 2 \frac{\bar{\omega}_\beta^2 M_{23} T_{23}}{M_{22} M_{33}} - \frac{T_{13}^2}{M_{11} M_{33}} - \frac{T_{23}^2}{M_{22} M_{33}} \\ B_4 &= f_4 - \frac{\bar{\omega}_\emptyset^2 M_{13}}{M_{11} M_{33}} - \frac{\bar{\omega}_\beta^2 M_{23}^2}{M_{22} M_{33}} + 2 \frac{M_{13} T_{13}}{M_{11} M_{33}} + 2 \frac{M_{23} T_{23}}{M_{22} M_{33}} \\ B_6 &= 1 - \frac{M_{13}^2}{M_{11} M_{33}} - \frac{M_{23}^2}{M_{22} M_{33}} \end{aligned}$$

in which

$$\begin{aligned} f_0 &= \bar{\omega}_\beta^2 \bar{\omega}_\emptyset^2 \bar{\omega}_\theta^2 \\ f_2 &= \bar{\omega}_\beta^2 \bar{\omega}_\emptyset^2 + \bar{\omega}^2 \bar{\omega}_\emptyset^2 + \bar{\omega}_\emptyset^2 \bar{\omega}_\theta^2 \\ f_4 &= \bar{\omega}_\beta^2 + \bar{\omega}_\emptyset^2 + \bar{\omega}_\theta^2 \end{aligned}$$

while $\bar{\omega}_\beta^2 = \omega_\beta^2 / \Omega^2$, etc.

The characteristic equation for the two-dimensional system is found to be

$$\sum_{k=0}^3 D_{2k} \lambda^{2k} = 0$$

where

$$\begin{aligned} D_0 &= f_0 - \bar{\omega}_\emptyset^2 h_a a_1^2 - \bar{\omega}_\beta^2 h_b b_1^2 \\ D_2 &= f_2 - \bar{\omega}_\emptyset^2 g_a \bar{x} a_1 - \bar{\omega}_\beta^2 g_b \bar{x} b_1 - h_a a_1^2 - h_b b_1^2 \\ D_4 &= f_4 - C_4 \bar{x}^2 - g_a x a_1 - g_b \bar{x} b_1 \\ D_6 &= 1 - C_6 \bar{x}^2 \end{aligned}$$

in which

$$h_a = \frac{M_{11}}{R^2 M_{33}} \quad h_b = \frac{M_{22}}{M_{33}}$$

$$g_a = 2 h_a A_1 \quad g_b = 2 h_b A_2$$

$$C_4 = \bar{\omega}_\emptyset^2 h_a A_1^2 + \bar{\omega}_\beta^2 h_b A_2^2$$

$$C_6 = h_a A_1^2 + h_b A_2^2$$

$$a_1 = A_1 (\bar{\omega}_\beta^2 l_{s_1} + r_m \bar{\omega}_\theta^2 l_{s_2}) - B \bar{\omega}_\theta^2 l_{s_2}$$

$$b_1 = A_2 (\bar{\omega}_\beta^2 l_{s_1} + r_m \bar{\omega}_\theta^2 l_{s_2}) + B \bar{\omega}_\theta^2 l_{s_2}$$

Equating D_0/D_6 to B_0/B_6 , D_2/D_6 to B_2/B_6 and D_4/D_6 to B_4/B_6 provides three relations in the three unknowns \bar{x} , l_{s_1} and l_{s_2} . If a_1 and b_1 are eliminated, the following equation for \bar{x} is obtained:

$$(r_1 t_2 - r_2 t_1)^2 + (r_1 s_2 - r_2 s_1)(t_2 s_1 - t_1 s_2) = 0$$

where

$$r_1 = - \left[h_a + \frac{h_b g_a^2}{g_b^2} \right] \quad r_2 = \left[\frac{\bar{\omega}_\theta^2}{\bar{\omega}_\beta^2} - 1 \right] h_a$$

$$s_2 = (\bar{\omega}_\beta^2 - \bar{\omega}_\theta^2) g_a \bar{x}, \quad s_1 = s_2 + \frac{2 h_b g_a F}{g_b^2 \bar{x}}$$

$$t_1 = (1 - C_6 \bar{x}^2) B_2/B_6 - f_2 + \bar{\omega}_\beta^2 F + \frac{h_b F^2}{g_b^2 \bar{x}^2}$$

$$t_2 = (1 - C_6 \bar{x}^2) (B_2 - B_0 / \bar{\omega}_\beta^2) / B_6 - f_2 + f_0 / \bar{\omega}_\beta^2 + \bar{\omega}_\beta^2 F$$

in which

$$F = f_4 - B_4/B_6 + (B_4 C_6/B_6 - C_4) \bar{x}^2$$

With some algebraic manipulation, a polynomial of fourth degree in \bar{x}^2 can be extracted from that equation. The value of \bar{x} is taken to be the square root of the smallest positive root of that polynomial. The original equations are then used to solve for a_1 and b_1 , from which l_{s_1} and l_{s_2} are readily obtained.

